An Integrated Experimental-Numerical Approach to Predictive Modelling of Fracture in Materials Subjected to Impact Loading

N. Petrinic[1], L.P. Weiss[3], P.R. Johnson[2], L. Wang[1], B.C.F. Elliott[1]

[1]Solid Mechanics Group, Department of Engineering Science, University of Oxford
Parks Road, Oxford OX1 3PJ, UK
[2]Numerical Analysis Group, Computing Laboratory, University of Oxford
Parks Road, Oxford OX1 3QD, UK
[3]Institut für Leichtbau und Kunststofftechnik, Technische Universität Dresden
01062 Dresden, Germany

ABSTRACT

Laboratory experiments of varied complexity and the corresponding numerical simulation procedures have been integrated to enable improved predictive modelling of fracture in materials subjected to impact loading. Application of this methodology which comprised a part of mechanical characterisation of an aluminium alloy has been presented in this paper. The results of uniaxial tensile tests at different rates of strain, fast crack growth and plate-bending and penetration experiments have been employed to direct the development of predictive modelling algorithms and identification of parameters required by the underlying mathematical equations through inverse modelling.

INTRODUCTION

State-of-the-art design of structures threatened by impact loading require the ability to predict material fracture – the breakage of atomic bonds at microscopic scale or the transition from continuum to discontinuum at macroscopic scale. In the case of design to withstand impact one of the most important design objectives is to improve the ability of given materials to dissipate kinetic energy possessed by colliding solid bodies or by rapidly flowing fluids following an explosion. The ability of solids to dissipate energy is related to their capacity to deform inelastically and/or their capability to fragment and dissipate the energy by sliding along thus created multiple interfaces. At both microscopic and macroscopic scales these phenomena are categorised as frictional processes which cause adiabatic heating and should be treated as coupled mechanical-thermal problems. These processes are complex and impossible to separate fully while characterising the behaviour of given materials experimentally. As a result, an integrated experimental-numerical approach to material characterisation for predictive modelling is required. Present efforts in establishing such integrated framework are outlined in this paper by focusing on material characterisation of an aluminium alloy for aerospace applications.

Material testing standards struggle to follow the advances in computational modelling as increasingly complex hypotheses on material behaviour are incorporated into newly developed models without comprehensible suggestions on experimental routes to quantifying the corresponding phenomena. This means that even the simplest of the experiments (e.g. uniaxial tension, three point beam bending) should be seen as the "validation tests" rather than treated as exercises in which intrinsic material properties could be measured directly. In this approach all material characterisation tests should be performed with the intention of simulating numerically the conducted experiments thus assuming the utilisation of calibrated sensors for integral and discrete measurements. Examples of integral measurement devices are load cells and contacting or non-contacting extensometers while discrete (point-wise) measurements are performed by means of optical

(high-resolution photographic equipment), infra-red (thermal imaging) and X-ray (2D and 3D tomography [5]) remote sensing devices using which full displacement and temperature fields representations can be established by interpolation.

Observations and measurements made during the experiments should be used to classify the material behaviour and enable the selection of existing numerical models or development of new ones. The term "numerical model" used here encompasses the discretisation method, kinematic and constitutive equations as well as partial differential equations solution algorithms since diverse combinations of these computational algorithms require different parameters in order to represent the observed material behaviour. Hence, the multi-action inverse modelling approach (depicted in *Figure 1*) to selecting the predictive modelling methodology as well as to designing the manufacturing processes to assist creation of new materials aimed at satisfying specific requirements.
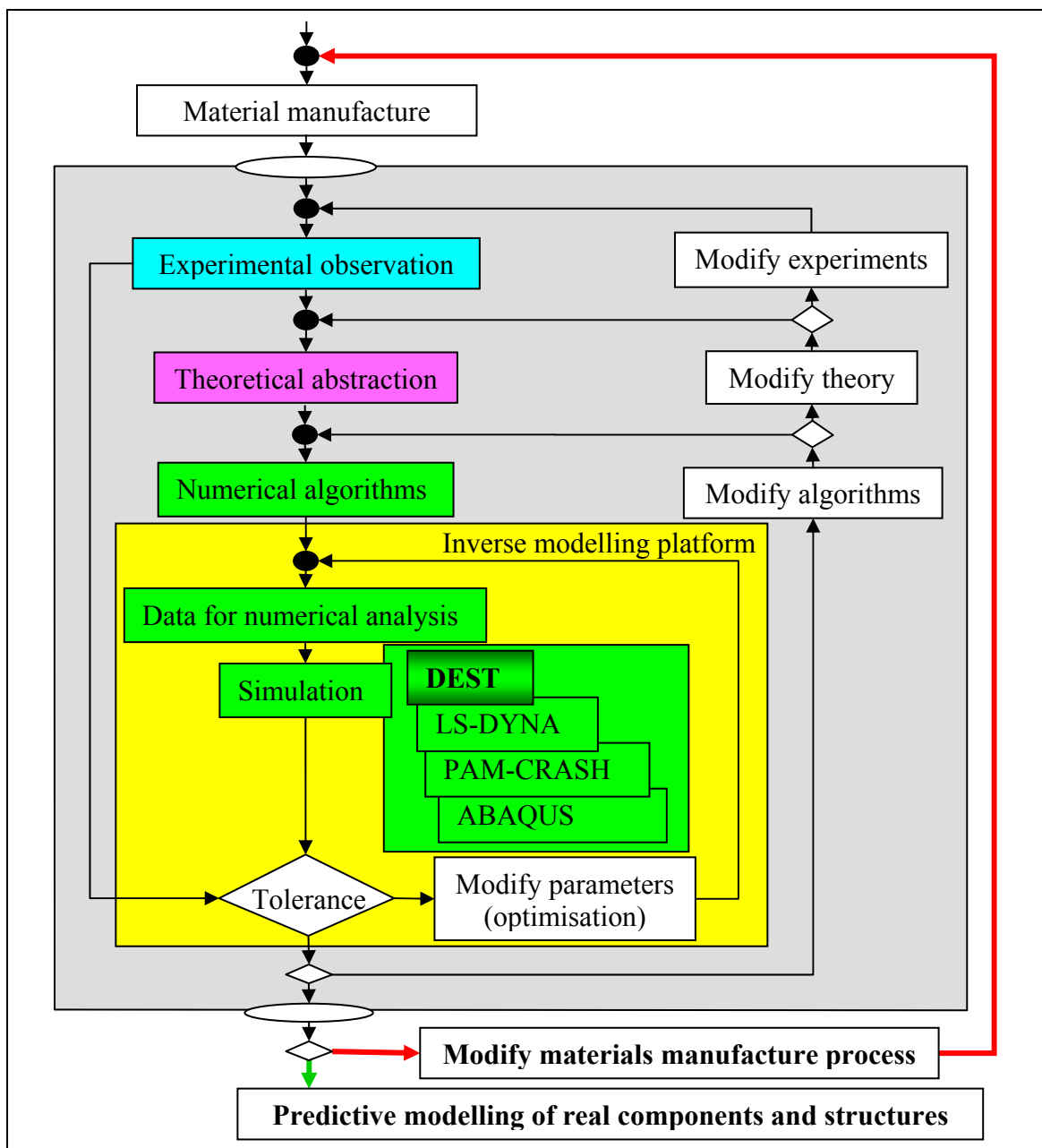

Figure 1: Integrated experimental-numerical approach to characterisation of materials

Modelling of material response to impact loading is widely performed by means of the finite element method involving some form of non-linear constitutive model with limiting strain, mesh refinement and element removal technique for simulation of fracture. In this paper, an improved damage mechanics based constitutive model and element splitting method in 3D is proposed that allows for material fracture to be simulated more accurately than the element removal technique.

In the next section examples of experiments used for selection of constitutive models and identification of model parameters for the investigated aluminium alloy are presented. Subsequent sections describe the selected numerical model and the employed inverse modelling procedures and their capability to simulate the material behaviour observed and quantified in the conducted laboratory experiments. Finally, the proposed 3D element splitting procedure is outlined and re-meshing operations around a crack plane are described for arbitrary tetrahedral meshes.

EXPERIMENTS FOR CHRACTERISATION OF MATERIAL FRACTURE

The following four types of experiments have been selected to assist the material characterisation for predictive modelling of impact penetration
   - uniaxial tension tests at three distinct rates of strain;
   - fast crack growth tests in preloaded panels;
   - low velocity plate impact bending test;
   - medium velocity impact penetration with two extreme projectile shapes (sharp cone and blunt cylinder).

Uniaxial tension experiments at three distinct rates of strain

Uniaxial tension testing at several distinct rates of strain represents the first step in characterisation of materials threatened by impact loading. The specimens whose geometry is depicted in *Figure 2* are normally used in experiments with metallic alloys. The data analysis of electronic signals recorded during tests at quasi-static, medium and high loading rates is illustrated in *Figure 3*, *Figure 4* and *Figure 5* respectively. At all loading rates the results of measurements are expressed in terms of stress-strain relationships which are used to postulate the constitutive response of the material under consideration. The investigated aluminium alloy exhibited an apparent strain rate independent response (*Figure 6*) but the experience of performing uniaxial tensile experiments at elevated temperatures [14] suggested that a temperature dependent elasto-viscoplastic constitutive model [1,12,13] capable of simulating the competing mechanisms of thermal softening and rate dependent strain hardening of a porous crystalline medium should be employed in simulations of conducted laboratory experiments.
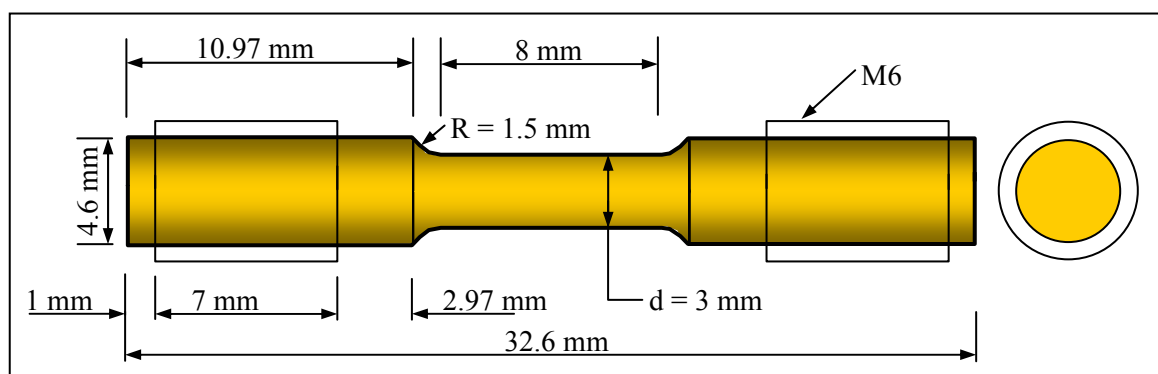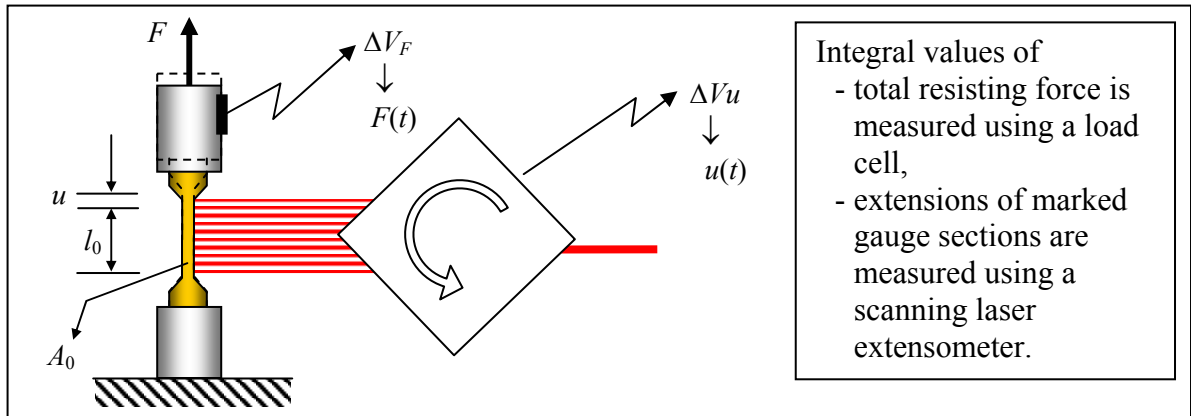

Figure 2: Uniaxial tension specimen (not to scale)

Integral values of
- total resisting force is measured using a load cell,
- extensions of marked gauge sections are measured using a scanning laser extensometer.

Figure 3: Quasi-static uniaxial tension testing

Integral values of
- total resisting force is measured using a load cell,
- extension of marked gauge section is measured using a linear voltage displacement transducer (LVDT).
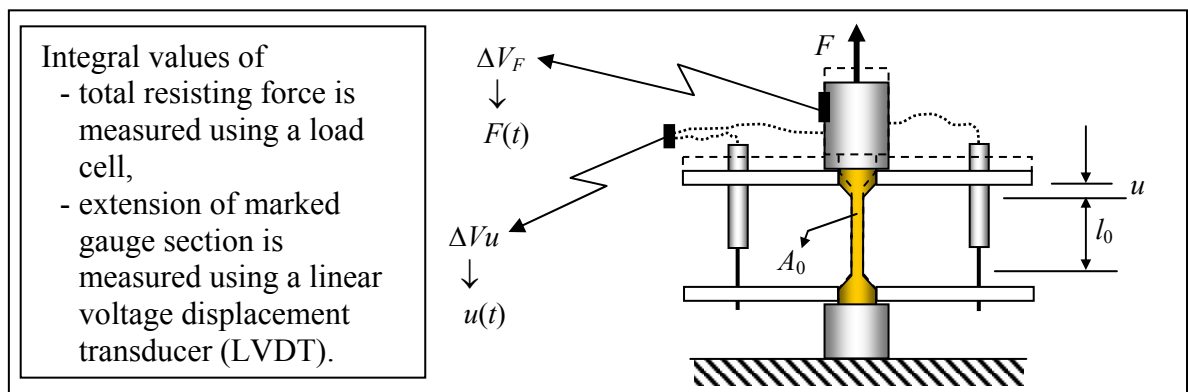
Figure 4: Medium rate uniaxial tension testing

Strains measured at strain gauge stations enable calculation of
- integral value of total resisting force as a function of time in the cross section at the interface with output bar (noted as F_{OUT})
- velocities of particles as functions of time at the interface with input bar (noted as v_{INP})and at the interface with the output bar (noted as v_{OUT})
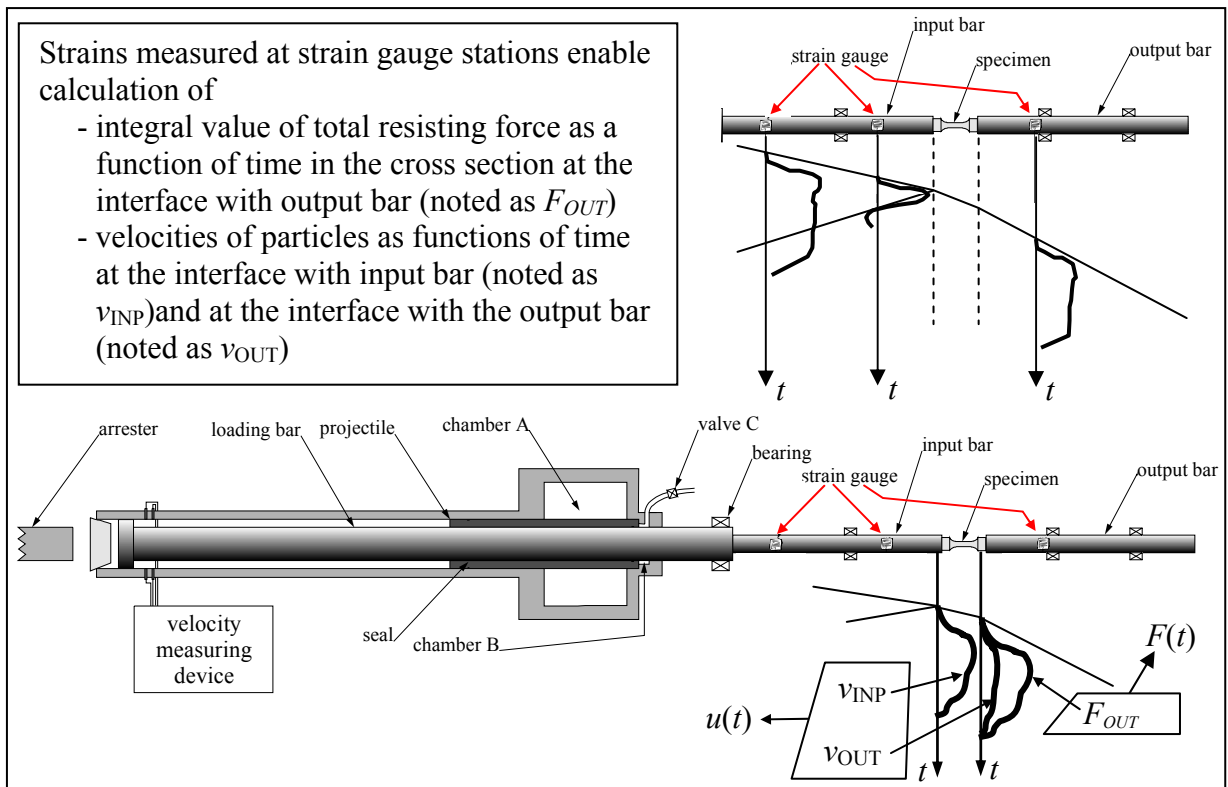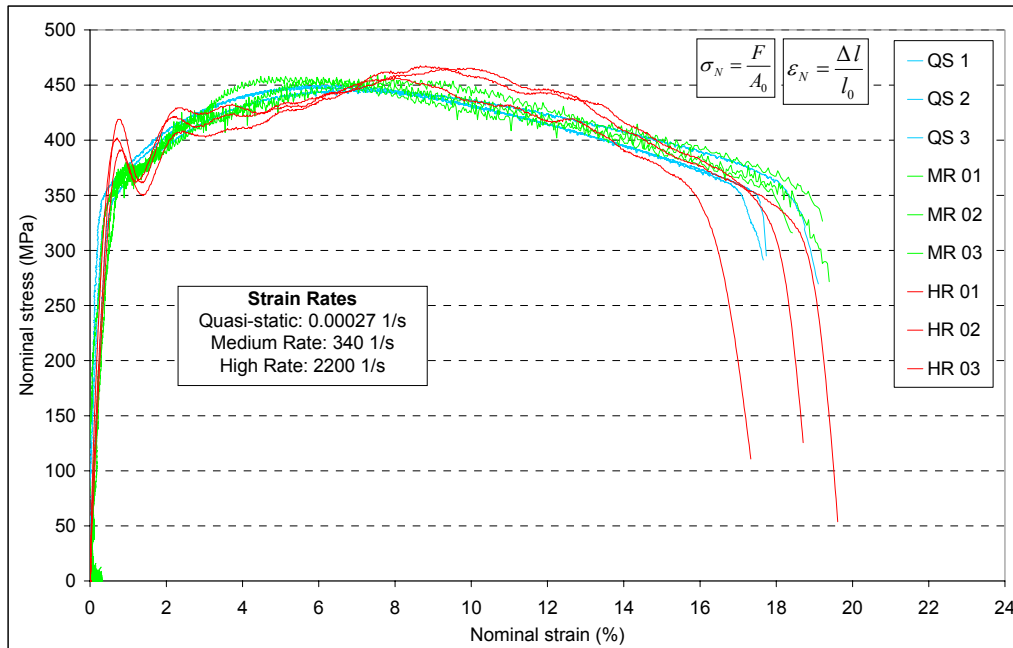
Figure 5: High rate uniaxial tension testing

Figure 6: Response to uniaxial tension testing at three distinct rates of strain

Fast crack growth experiments

The specimen geometry used to study fast ductile crack propagation and the testing rig are depicted in *Figure 7* and *Figure 8*. In the experiment the specimen is instrumented with an array of strain gauges and preloaded to a stress approaching two thirds of the yield stress or one third of the tensile strength of the material. The preload is applied to the specimen by means of two pneumatic cylinders with a capacity of 80 kN. Having two rather than one cylinders provides a symmetrical configuration in which the centre of the specimen does not move significantly during the test. The stored energy of the pressurised gas ensures that the applied forces remain constant during crack growth. The crack is started to grow by a wedge-tipped impactor bar which is held lodged inside the notch at one side of the specimen. It is instrumented with a strain gauge used to trigger the high-speed camera with which the process is photographed at up-to 35,000 frames per second (*Figure 9*). This bar is accelerated against the specimen following impact by a projectile bar contained inside a gas gun and running on nylon bushes. The impact velocity, measured with light curtains, is up-to 25 m/s. A high-speed data acquisition system is used to record the signals from strain gauges fixed to the specimen.
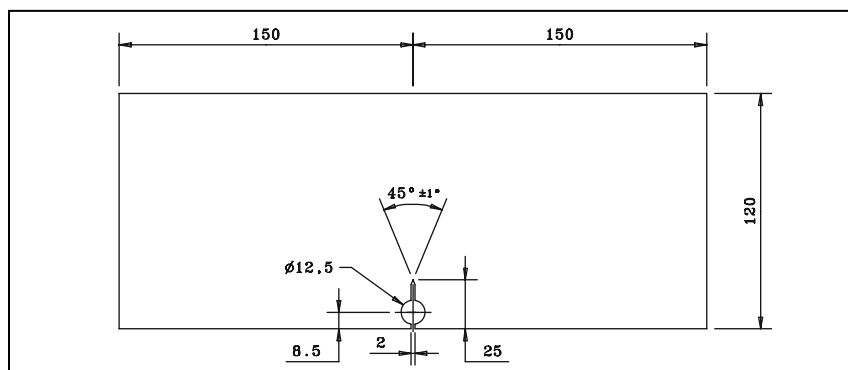

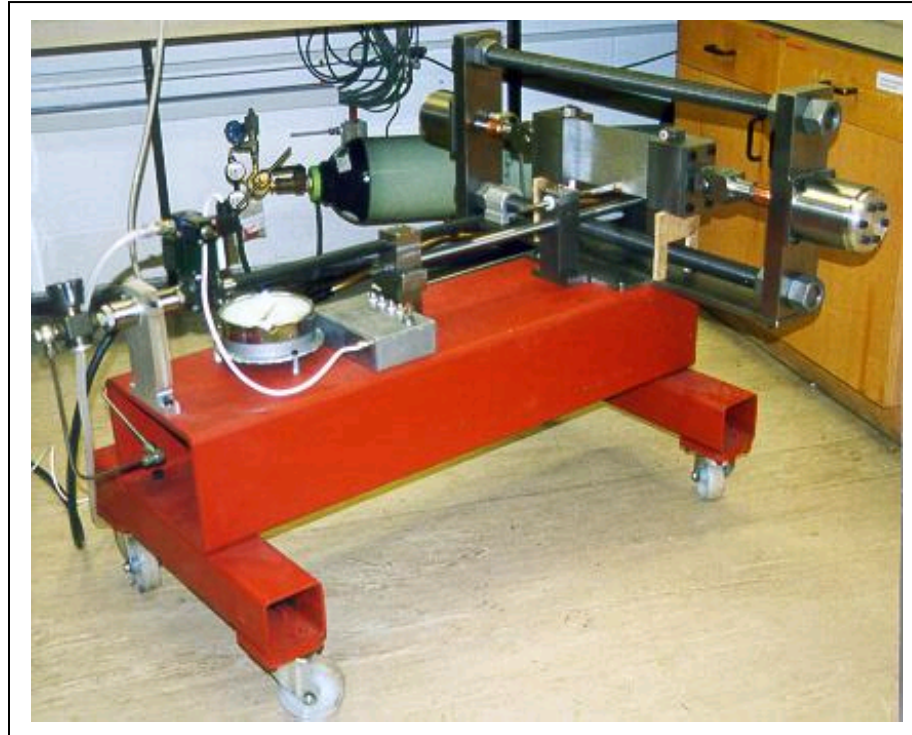*Figure 7: Fast crack growth specimen (nominal thickness 3 mm)*

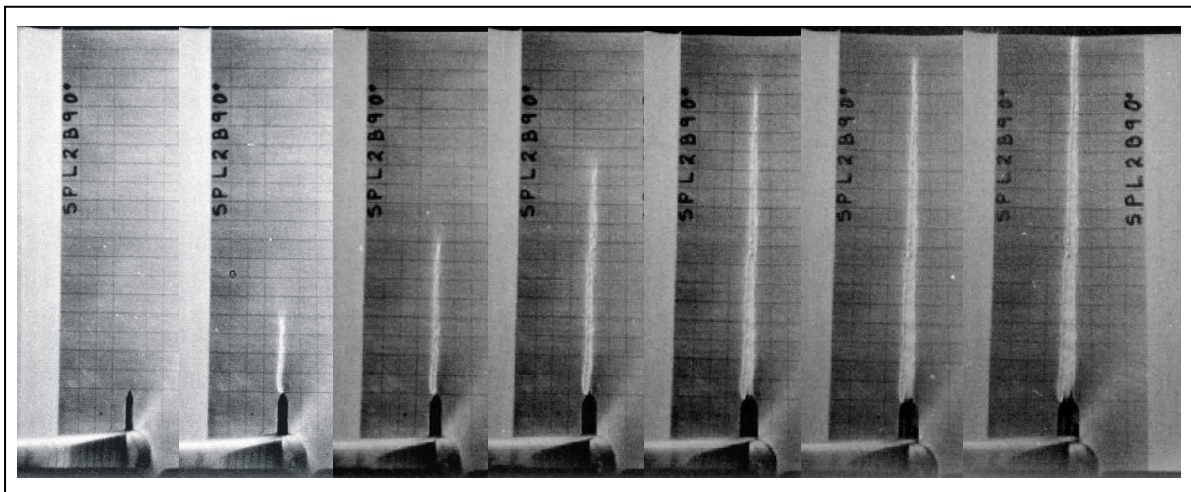

Figure 8: Fast crack growth loading device

Figure 9: Example of fast crack growth in aluminium panel

Low velocity plate impact bending experiment

A set of plate impact bending experiments at low velocity has been performed using a small gas gun capable of firing long rod projectiles at velocities of up-to 13 m/s. In these experiments the chosen projectile is aimed to impact an instrumented rod (the impactor bar) of the same material and dimensions as the projectile. During impact the kinetic energy of the projectile is fully transferred to the impactor bar which continues to travel virtually unstressed towards the target plate (*Figure 10*). The velocity of the impactor bar is measured using light curtains just before impacting the target plate. The target plate is placed to lean against a long instrumented tubular support which is free to move in the direction of impact.
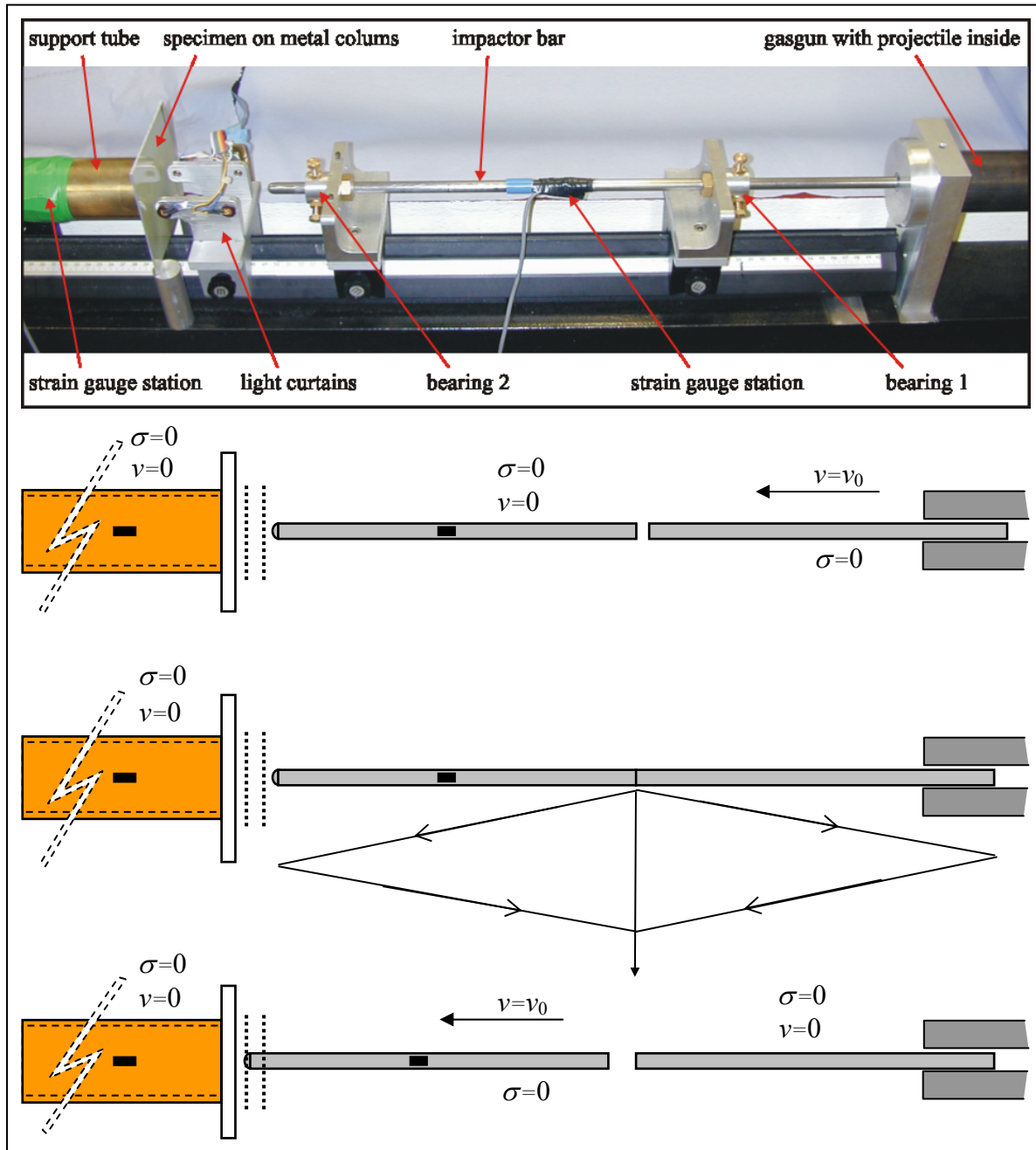

Figure 10: Momentum transfer from projectile to impactor bar

It is assumed that both the impactor bar and support tube only deform elastically during impact. The instrumentation (strain gauge stations denoted in *Figure 10 - Figure 13* by black rectangles) on the impactor bar and support tube enables the measurement of the travelling elastic stress waves caused by the load exerted by impactor bar against the target plate (*Figure 11*).
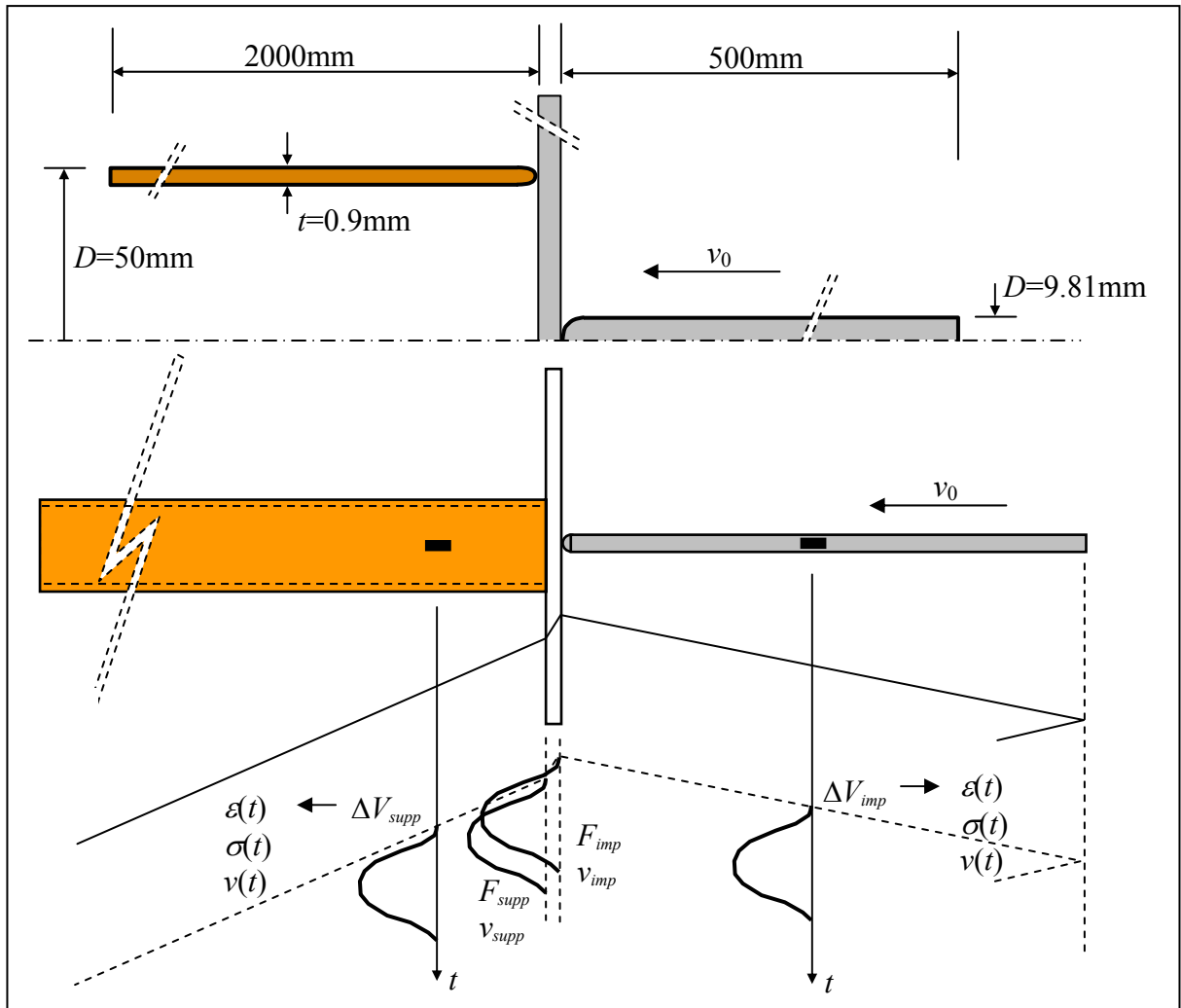

Figure 11: Measurements of stress waves propagation in impactor bar and support tube

The calculation of the applied impact force and the force transmitted through the specimen (or the reaction force measured on the support tube) in addition to the plate deflection as functions of time is described in *Figure 12*. The employed analytical method relies upon the solution of the wave equation which describes the dynamic equilibrium in 1D elastic continuum [6,13]. The solution based upon the method of characteristics results in the evaluation of the impact force at the tip of the impactor bar as well as along the ring of the support tube as functions of time. At the same time the velocities of both the tip of the impactor bar and the ring of the support tube are obtained as functions of time. By integrating the tip and ring velocities with respect to time and subtracting them the plate deflection is obtained as a function of time.
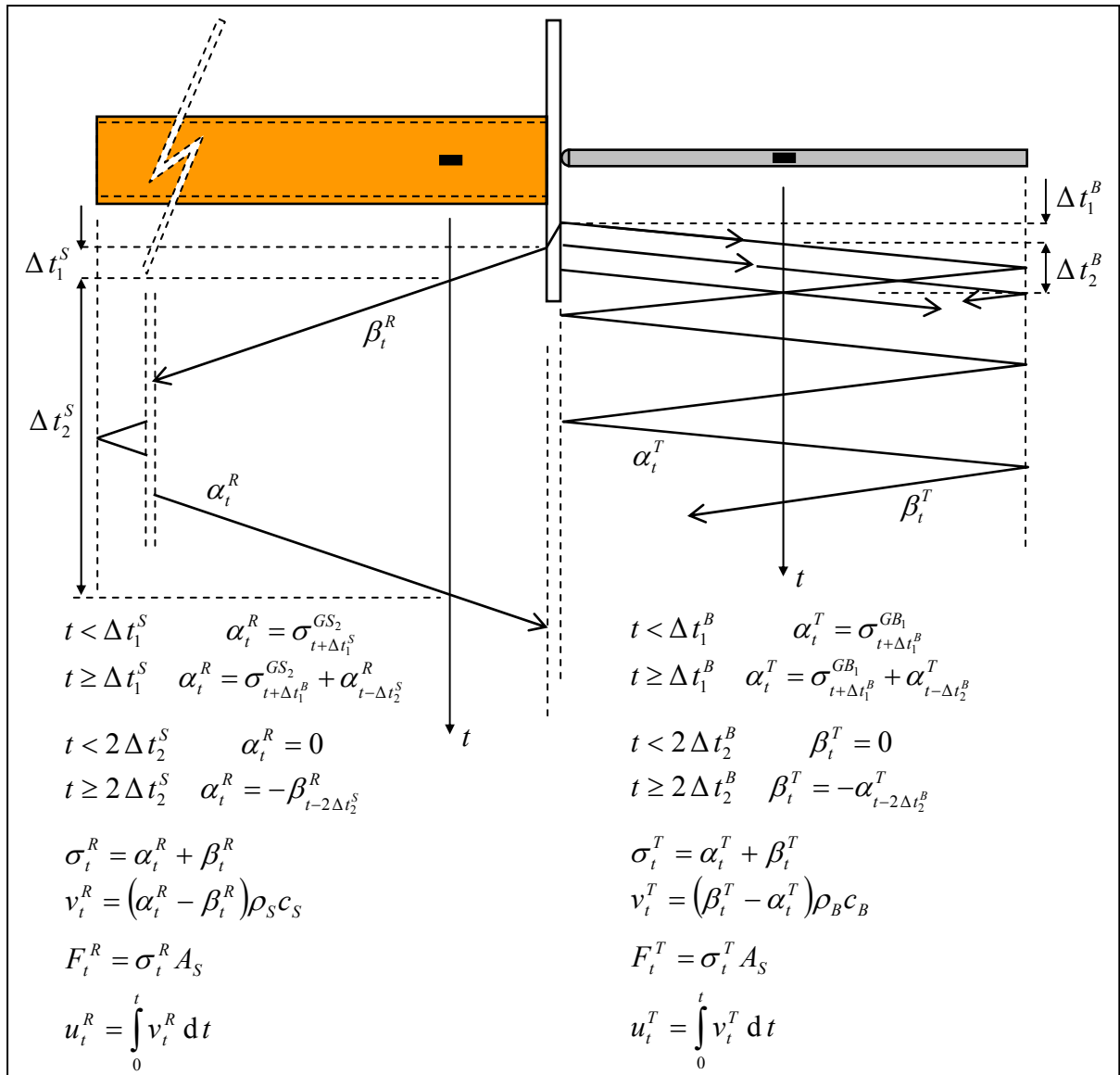
Figure 12: Analysis of motion caused by impact

$$t < \Delta t_1^S \qquad \alpha_t^R = \sigma_{t+\Delta t_1^S}^{GS_2}$$
$$t \geq \Delta t_1^S \quad \alpha_t^R = \sigma_{t+\Delta t_1^B}^{GS_2} + \alpha_{t-\Delta t_2^S}^R$$

$$t < 2\,\Delta t_2^S \qquad \alpha_t^R = 0$$
$$t \geq 2\,\Delta t_2^S \quad \alpha_t^R = -\beta_{t-2\Delta t_2^S}^R$$

$$\sigma_t^R = \alpha_t^R + \beta_t^R$$
$$v_t^R = \left(\alpha_t^R - \beta_t^R\right)\rho_S c_S$$

$$F_t^R = \sigma_t^R A_S$$

$$u_t^R = \int\limits_0^t v_t^R \, \mathrm{d}t$$

$$t < \Delta t_1^B \qquad \alpha_t^T = \sigma_{t+\Delta t_1^B}^{GB_1}$$
$$t \geq \Delta t_1^B \quad \alpha_t^T = \sigma_{t+\Delta t_1^B}^{GB_1} + \alpha_{t-\Delta t_2^B}^T$$

$$t < 2\,\Delta t_2^B \qquad \beta_t^T = 0$$
$$t \geq 2\,\Delta t_2^B \quad \beta_t^T = -\alpha_{t-2\Delta t_2^B}^T$$

$$\sigma_t^T = \alpha_t^T + \beta_t^T$$
$$v_t^T = \left(\beta_t^T - \alpha_t^T\right)\rho_B c_B$$

$$F_t^T = \sigma_t^T A_S$$

$$u_t^T = \int\limits_0^t v_t^T \, \mathrm{d}t$$

The loading apparatus had been particularly designed for performing plate impact bending experiments with relatively long collision interaction times. The illustration in *Figure 13* confirms that the impactor bar rebounds and impact ceases before the stress wave reflected from the free end of the support tube reaches the strain gauge station (denoted as GS$_2$ in *Figure 13*) near the target plate. This enables more accurate calculation of the reaction forces because the principle of superposition of travelling waves is not required.
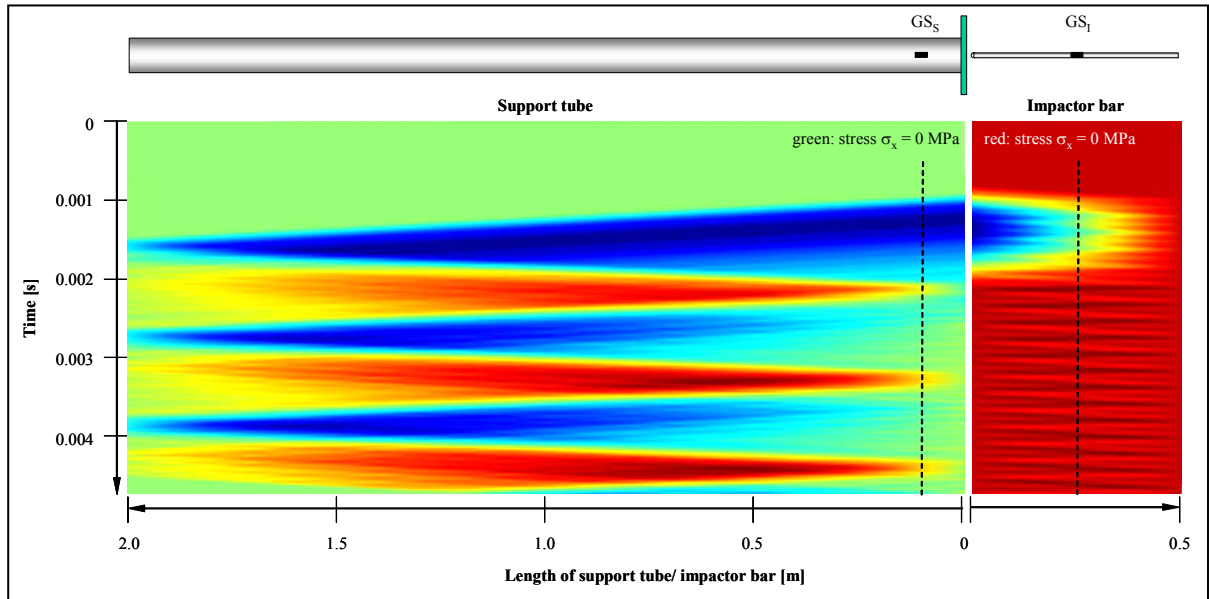
Figure 13: History of distribution of axial stress in impactor bar and support tube

Good repeatability has been achieved thus providing confidence in the reliability of the loading apparatus and measurement systems. The results of plate impact bending tests at low velocity are summarised in *Table 1* and *Table 2*.

The total energy dissipated through such localised inelastic deformation of the target plate was calculated by monitoring the kinetic and strain energy of the impactor rod and support tube as well as strain energy of the deflected target as illustrated in (*Figure 14*).

Post-impact visual examination of impacted plates (*Figure 15*) suggested that extensive but localised deformation had been caused by the applied impact loading. Further measurements of residual deflections are planed in order to provide additional data on energy dissipation during impact.

Table 1: Low velocity plate impact bending – specimen geometry

Specimen	Height (mm)	Width (mm)	Thickness (mm)
CRE 3	99.97	99.98	1.46
CRE 4	99.97	99.99	1.47
CRE 5	99.99	100.00	1.46

Table 2: Low velocity plate impact bending – energy dissipation

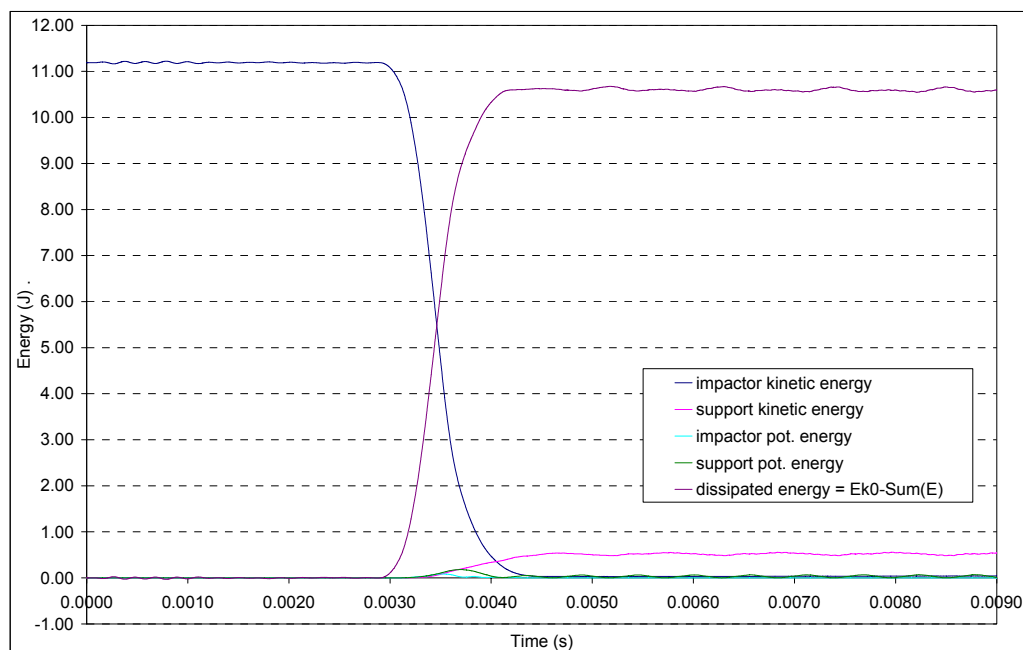| Specimen	Initial kinetic energy (J)	Dissipated Energy (J)	Ratio
CRE 3	11.716	10.425	88.9 %
CRE 4	11.146	9.860	88.4%
CRE 5	11.597	10.318	88.9%

Figure 14: Energy balance in a typical low velocity plate impact bending test

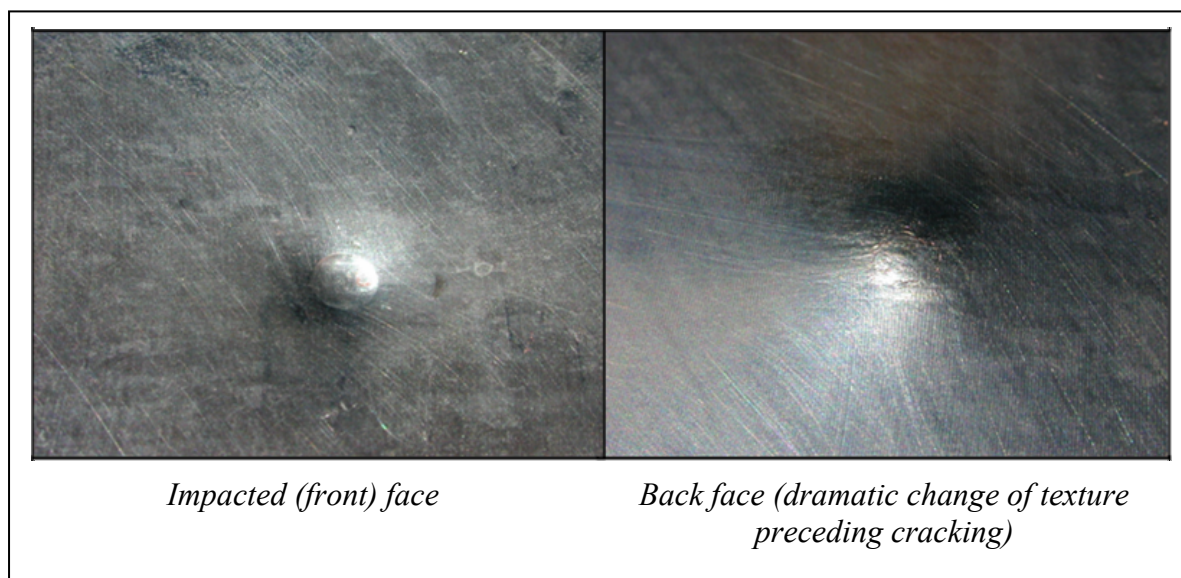|	
Impacted (front) face	*Back face (dramatic change of texture preceding cracking)*

Figure 15: Typical deformation of impacted plates

Medium velocity impact penetration experiments

A set of experiments at medium velocity (up-to 100 m/s) has been performed in order to observe the ability of the material to resist the penetration of impacting projectiles made up of different shapes at velocities comparable to those threatening real aircraft components in service. Two extreme projectile shapes have been investigated – sharp conical and blunt flat cylindrical projectiles of the same total mass (*Figure 16*). The sharp conical projectile was expected to cause tearing while the blunt flat projectile was expected to cause plugging. The circular ring support (*D*=80mm, *r*=6mm) was intentionally left incomplete (by 60°) in order to enable visualisation of specimen deflection. The experiment design which involved finite element simulations of the planned tests also suggested that fracture generated by impact

would run towards the missing part of the ring support which allowed for better observation of the material fracture phenomena.
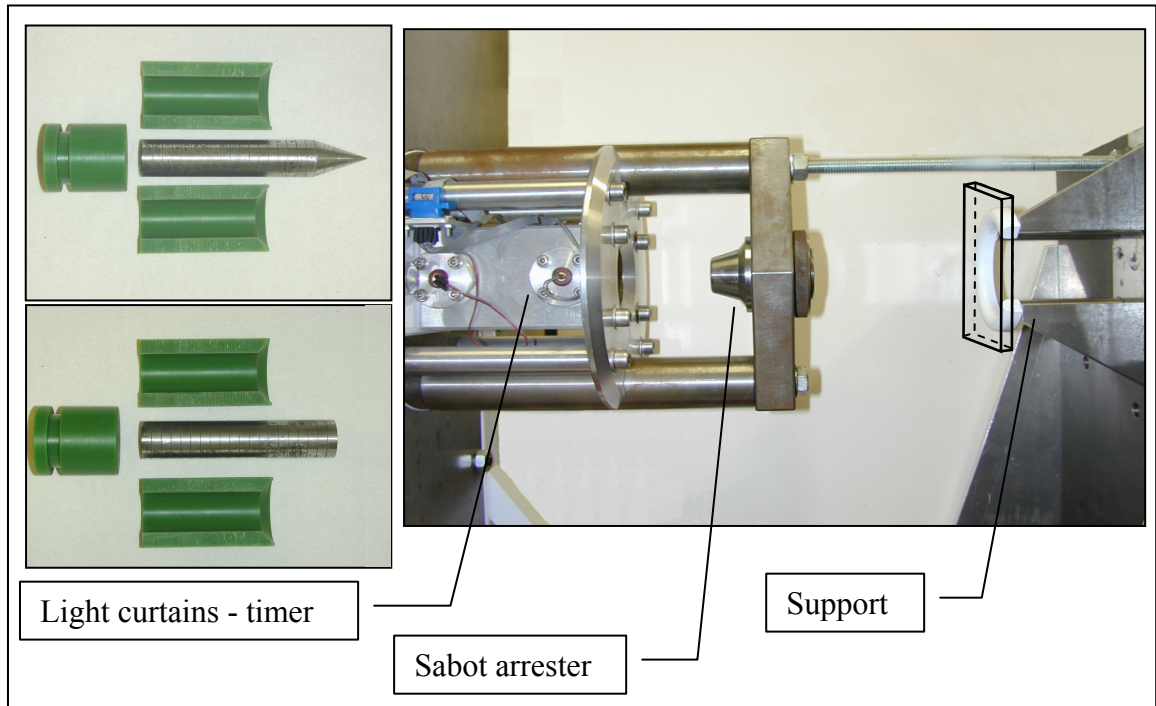
Figure 16: Experimental setup for medium velocity impact

The tests were recorded using a high-speed camera. Approximately 220 frames were recorded on a high sensitive 35 mm B/W film during each test (*Figure 17*). The frames were digitised in order to enable digital image processing for evaluation of projectile velocity and plate deflections as functions of time. A typical sequence of digitised images which provided data for calibration and subsequent measurement of monitored quantities is illustrated in *Figure 18*.

The impact force as a function of time was calculated from the change in momentum of the projectile. The corresponding change in kinetic energy of the projectile is calculated in order to estimate the energy dissipation due to inelastic deformation of the tested specimen. The initial approximation applied in this investigation was based on the assumption that the stored elastic energy is small compared to the dissipated energy. A typical set of results is presented in *Figure 19*.

The tearing threshold was for conical projectile at impact velocity of 49 m/s while the plugging threshold was for blunt flat projectile at impact velocity of 77 m/s. The most important observation was the different fracture mechanism. For the conical impactor the plate failed through radial hole opening and petalling whereas the plate impacted with the flat projectile failed by shear fracture. The tests setup and results data are summarised in

Table 3, *Table 4* and *Table 5*. Damage patterns corresponding to the critical cases reported in *Table 5* are depicted in *Figure 20*.
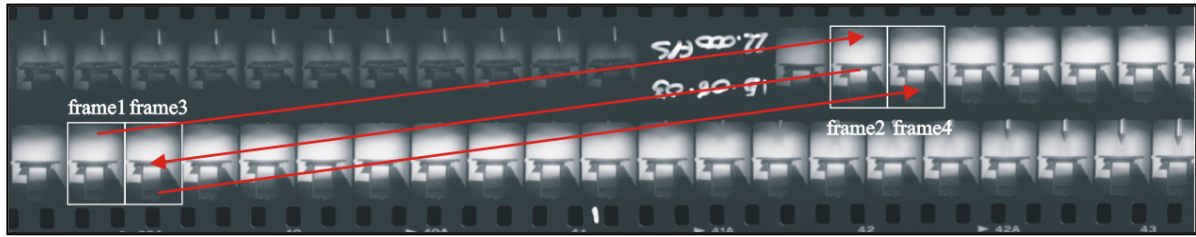
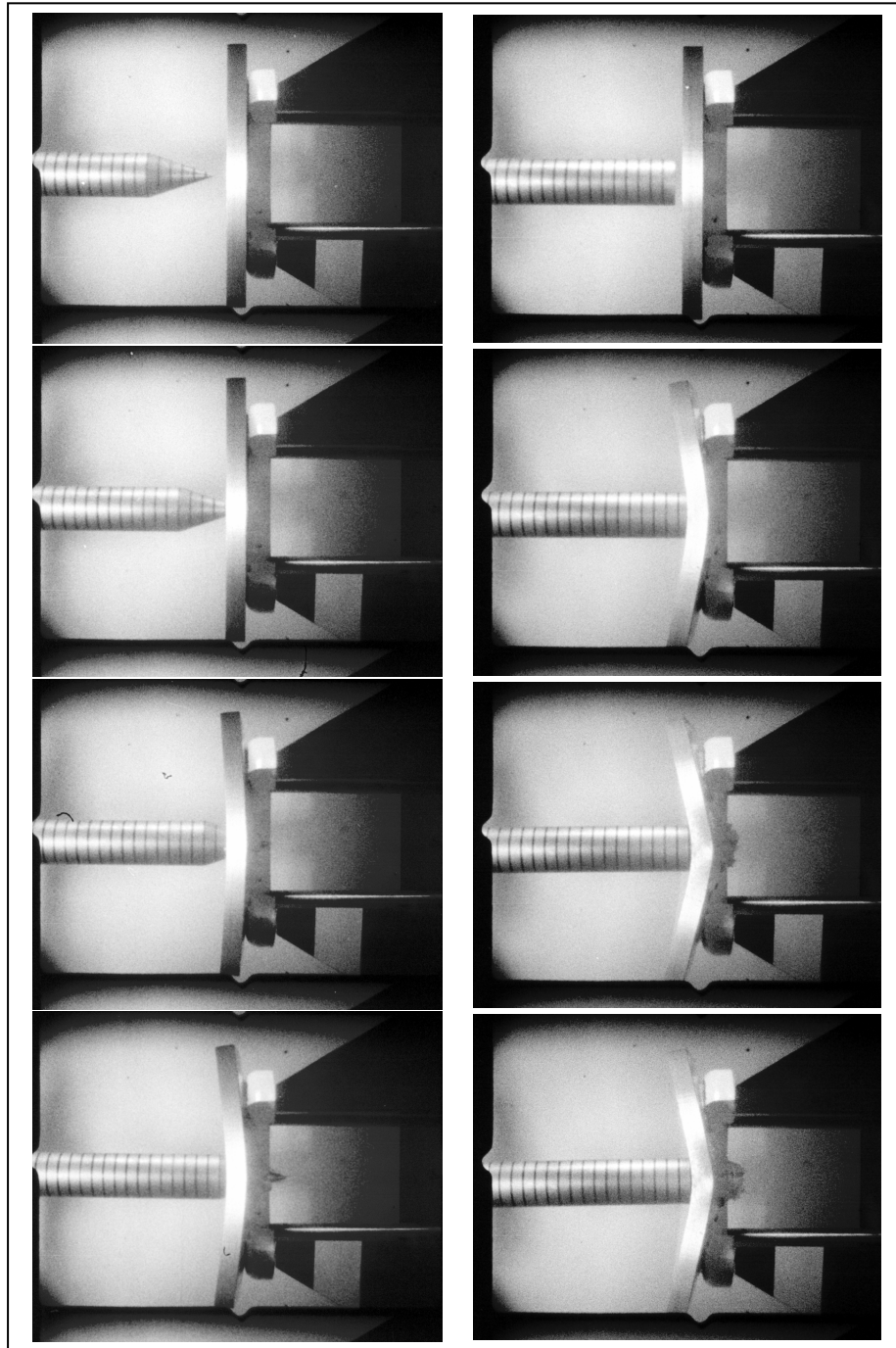*Figure 17: Segment of the film recorded using high-speed camera*

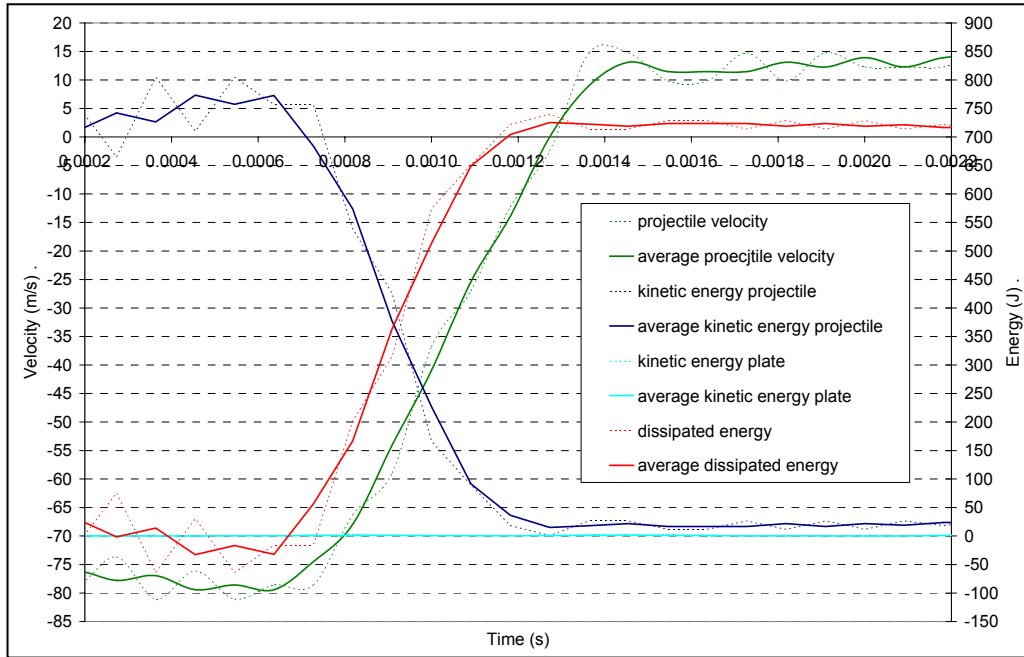*Figure 18: Typical results of medium velocity impact tests*

Figure 19: Projectile velocity and energy dissipation in a typical medium velocity impact test

Table 3: Medium velocity plate impact bending – specimen geometry

Specimen	Thickness (mm)	Length (mm)	Width (mm)	Mass (g)
CRE1	7.50	100.0	100.0	211.8
CRE2	7.51	100.0	100.0	211.9
CRE3	7.51	100.0	100.0	211.9
CRE4	7.50	100.0	100.0	211.8
CRE5	7.48	100.0	100.0	211.4

Table 4: Medium velocity plate impact bending – test data

Specimen	Projectile shape	Projectile mass (g)	Velocity (m/s)
CRE1	conical	242.9	49
CRE2	flat cylindrical	242.2	89
CRE3	conical	245.2	73
CRE4	flat cylindrical	242.6	74
CRE5	flat cylindrical	242.2	77

Table 5: Medium velocity plate impact bending – critical cases

Specimen	Kinetic energy (J)	Dissipated energy (J)	Ratio (%)	Max contact force (kN)
CRE3	740	718	97	42
CRE5	811	808	99	56

Figure 20: Critical damage patterns

CONSTITUTIVE MODELS AND MATERIAL FRACTURE

The constitutive model for metallic alloys employed in this study is motivated by the investigation of dynamic ductile damage [1,13]. In the proposed model the material response to rapidly imposed deformation is formally expressed in the following rate form

$$\overset{*}{\sigma}(t) = \Sigma[\sigma(\tau),\ \varepsilon(\tau),\ d(\tau),\ w(\tau),\ \theta(\tau),\ \alpha(\tau),\ \kappa(\tau),\ \{D\}],\quad -\infty < \tau \leq t \tag{1}$$

where σ is the Cauchy (true) stress, $\overset{*}{\sigma}$ is the objective rate of Cauchy stress tensor, Σ is the functional of deformation history, ε is the true strain tensor, d is the rate of deformation tensor, w is the spin tensor, θ is the temperature, α is the back stress, κ is the isotropic hardening and D is the internal isotropic damage scalar variable. The algorithmic implementation of this functional follows from the energy considerations encompassed by the fundamental principles of thermodynamics with internal variables [9,10] and additive decomposition of the velocity gradient into its elastic and inelastic parts [2,3].

In the case of aluminium the main focus is on providing a regularised damage evolution within the adopted isotropic-elastic-viscoplastic constitutive model with stress based yield criteria. The evolution of damage follows from the assumption of void growth in a rate dependent metallic alloy such that the rate of damage is

$$\dot{D} = \sinh\left[\frac{2(2m-1)p}{2(2m+1)\sigma'_{ef}}\right]\left[\frac{1}{(1-D)^m} - 1 + D\right]d^{pl} \tag{2}$$

where

$$p = \frac{1}{3}\text{tr}[\sigma] \tag{3}$$

is the hydrostatic pressure (or the means stress), and

$$\sigma'_{ef} = \sqrt{\frac{3}{2}(\sigma':\sigma')} \tag{4}$$

is the Von Mises effective stress, and

$$d^{pl} = \dot{\lambda} \tag{5}$$

is the effective plastic rate of deformation, $\dot{\lambda}$ is the plastic multiplier which follows from satisfying the consistency condition of the underlying viscoplastic constitutive equations [1], while the scalar function m which controls the rate of damage evolution is given by

$$m = C_{21}L_c + C_{22} \tag{6}$$

in which L_c is the element's characteristic length, i.e. the size of the integration domain in the direction of maximum principal rate of plastic strain d_1^{pl} (*Figure 21*), while C_{21} and C_{22} are the material parameters that need to be determined by comparison against experimental data. The introduction of such a length scale in the expression for evolution of damage enables an accurate simulation to be performed of the reduction in material resistance to continuing deformation which precedes fracture in metallic plies. This reduction ensures the correct energy dissipation per unit volume of the representative volume element V and energy release rate per fracture surface area A_c.

Further study will address the competing mechanisms of rate dependent hardening and thermal softening at high loading rates which the chosen material model is capable of simulating.
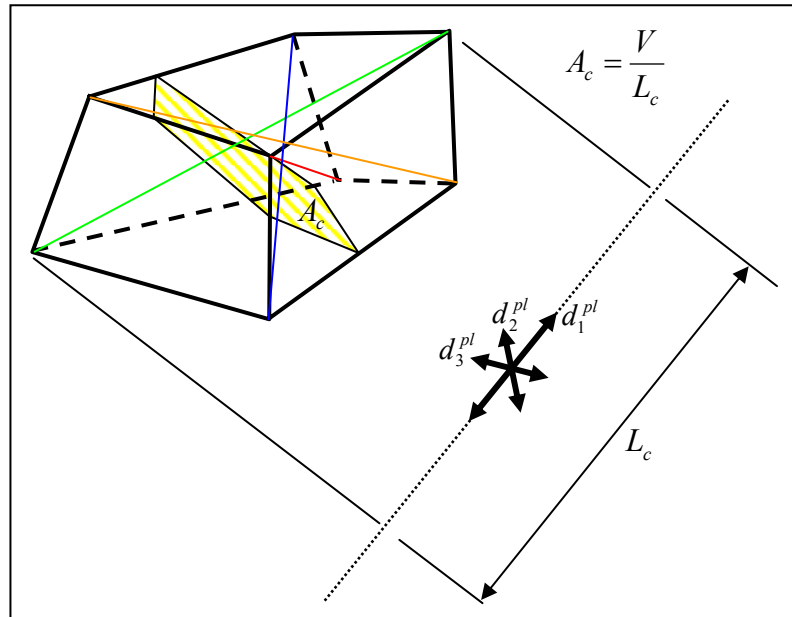

Figure 21: Characteristic length of damaged element and corresponding fracture surface

INVERSE MODELLING FOR PRAMETERS IDENTIFICATION

Let the set of material parameters which need identifying be denoted by a point in parameter hyperspace

$$\boldsymbol{p} = (p_1, p_2, \ldots, p_n) \subset \boldsymbol{P} \tag{7}$$

Given a Dirichlet boundary condition (i.e. the velocity boundary condition measured during the experiment) then the Neumann boundary condition (total resisting force provided by the specimen under tensile loading) for the given domain is obtained numerically and its variation with the parameters is expressed as follows

$$f(\boldsymbol{p}) = f(\boldsymbol{p}, v(t), t) \tag{8}$$

An objective function that measures the difference between the experimentally obtained and numerically simulated reaction force histories in a least squares sense is formulated as follows

$$J(\mathbf{p}) = \frac{1}{2} \left\| f(\mathbf{p}) - \hat{f} \right\|_Y^2 \tag{9}$$

The goal of the inverse modelling exercise is the optimal set of parameters $\boldsymbol{p}^*$, achieved when the objective function is at a global minimum and can be expressed by

$$\boldsymbol{p}^* = \mathbf{argmin}[J(\boldsymbol{p})] \tag{10}$$

or by

$$\exists \boldsymbol{p}^* \subset \boldsymbol{P} \in \forall \boldsymbol{p} \subset \boldsymbol{P} : J(\boldsymbol{p}) \geq J(\boldsymbol{p}^*) \tag{11}$$

Initially, a value of the objective function is obtained at the starting point (a given parameter set, estimated based on experience or guessed).

From the initial position in parameter space the computation towards the optimal one is carried out by the search algorithm. In this case it is a first order method based on a gradient based polynomial approximation linesearch update. Steps are completed after a sufficient decrease in the value of the objective function at the current parameter, which is further constrained to never increase between increments.

In the current implementation, derivatives of the objective function are evaluated using a central finite differencing procedure. This is found to be highly inaccurate due to the pollution of this result with noise. An alternative method of calculating derivatives via semi-analytical differentiation of the underlying system of equations is under development. Early results suggest this route is not as susceptible to noise problems.

Since the temporal locations of available experimental and numerical results do not necessarily coincide, the numerical and experimental results are linearly interpolated and the sum of squares of differences is calculated. This is the objective function used to evaluate the parameters.

Each inverse modelling simulation was set to terminate when a step size of less than 0.1 % of the current value of all parameters was reached. This gave reasonable execution times while reaching an accuracy far outweighed by other sources of error in the experiment. Optimisations were repeated from a variety of starting positions in order to ameliorate the effects of local minima. Each of these was found to terminate in a relatively small area of parameter space, giving high confidence in the results obtained.

An example of convergence in model parameters is presented in *Figure 22*. The consequent improved simulation results in expressed in terms of force-extension curves for uniaxial tension experiments at high rates of strain are presented in *Figure 23*.
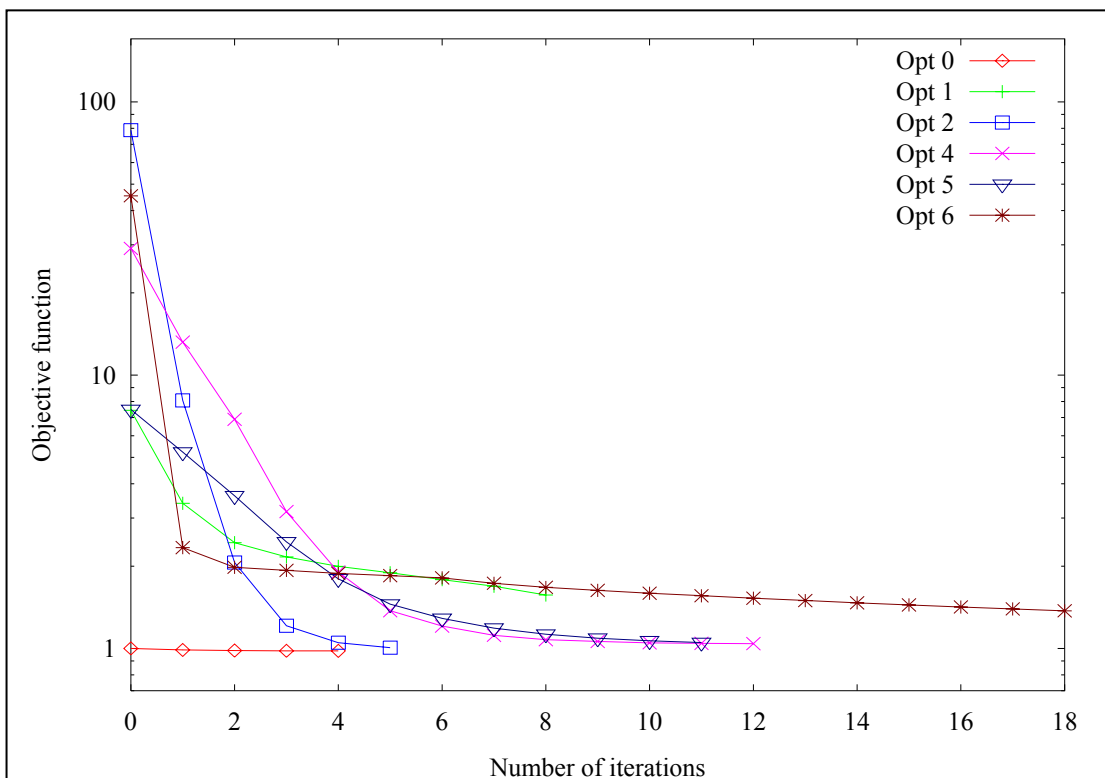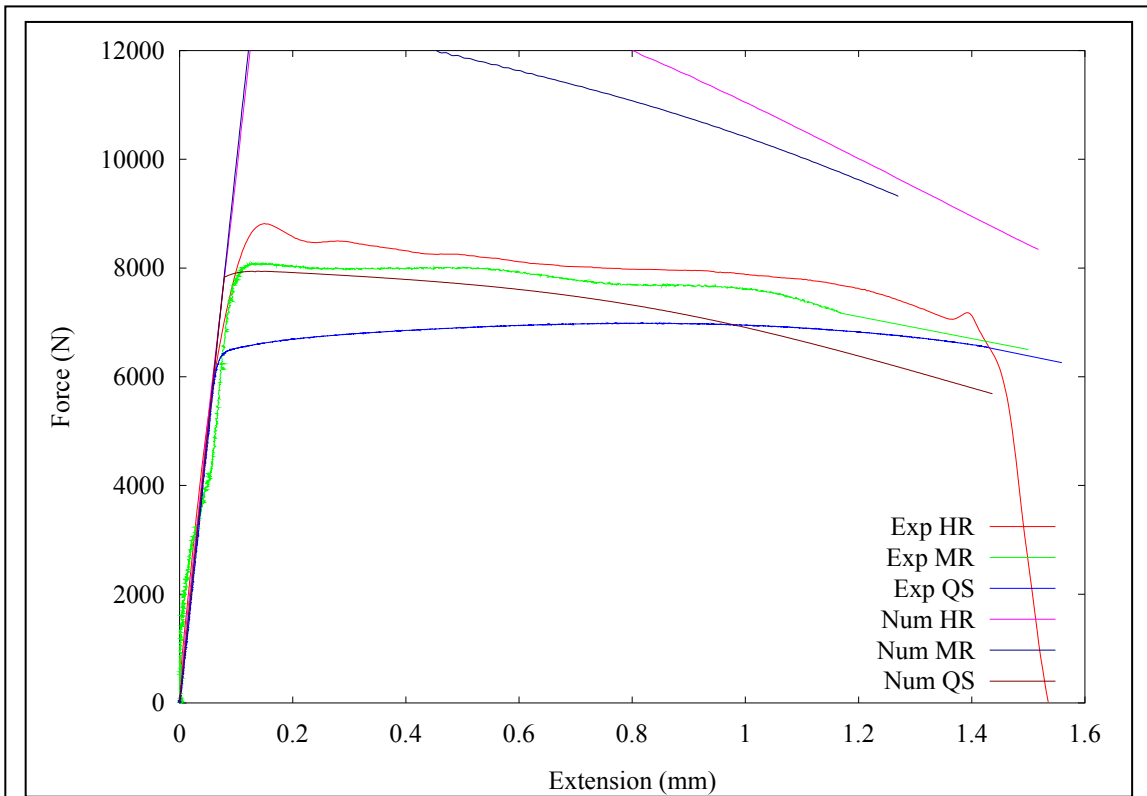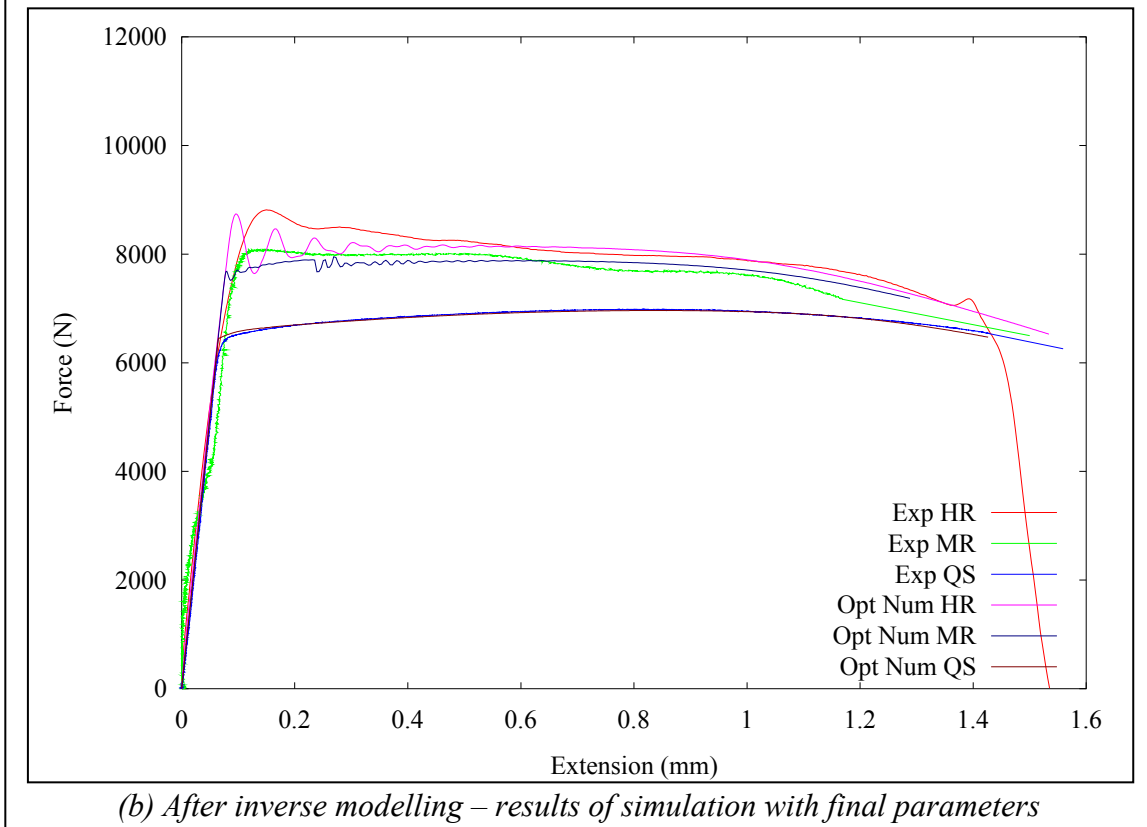

Figure 22: Model parameters convergence

(a) Before inverse modelling – results of simulation with initially guessed parameters

(b) After inverse modelling – results of simulation with final parameters

Figure 23: Improvement in simulation results following identification of optimal model parameters by inverse modelling

NUMERICAL MODELS OF CONDUCTED EXPERIMENTS

The numerical model illustrated in *Figure 24* and *Figure 25* has been used for simulation of uniaxial tension tests. The geometry reflects the applied gripping method while the boundary conditions idealise the applied loading conditions. The boundary conditions recorded in experiments performed at different loading rates are applied in the model in order to impose the observed deformation regime. The reported resisting force histories are used for comparison against the calculated reaction forces on the supported boundary in the model. A set of typical results following a simulation of uniaxial quasi-static and high rate tension tests are presented in *Figure 26* and *Figure 27*. In *Figure 26* the extensions are compared with those of marked regions within the gauges section of the specimen. In *Figure 27* several models of different mesh densities are compared against the experiments in order to show that the employed numerical models are insensitive of element size. Minimisation of the error between experimental and such obtained numerical results should yield the identification of constitutive parameters required to simulate accurately more complex loading conditions applied upon more elaborate geometries.
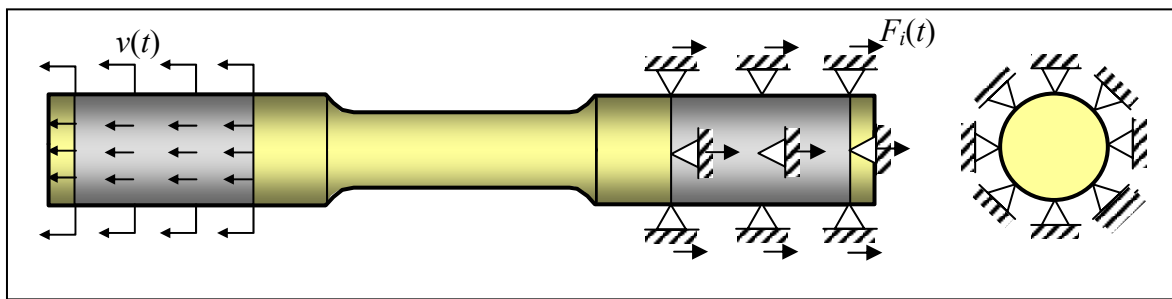

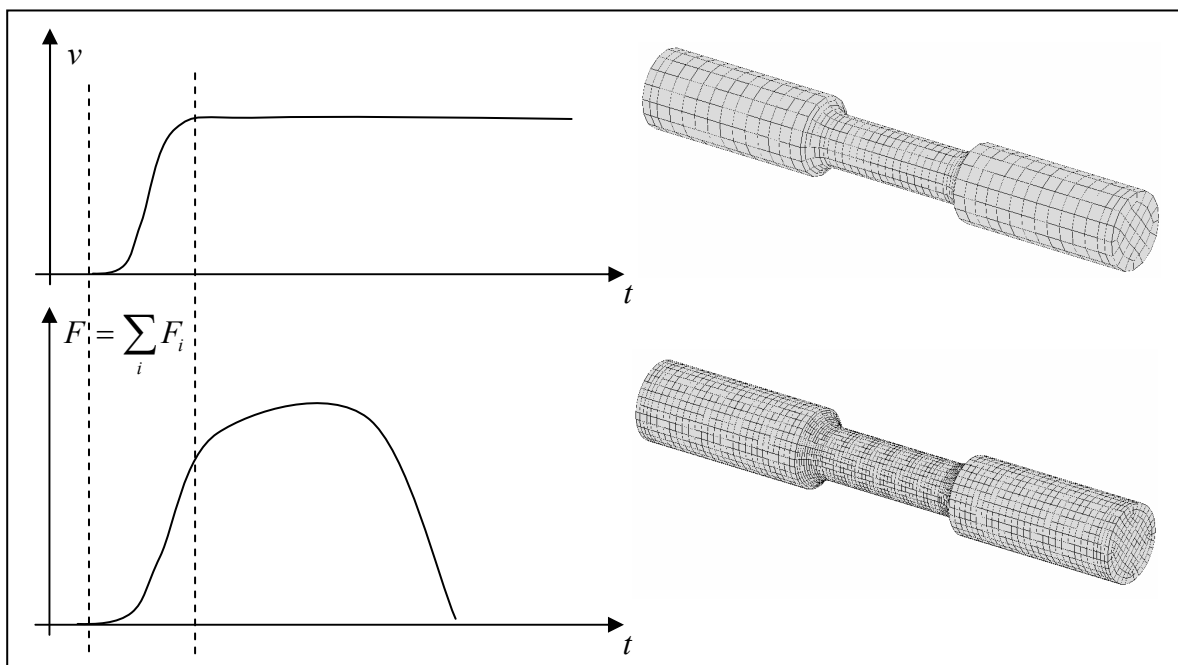*Figure 24: Model geometry and boundary conditions*

Figure 25: Idealised shape of prescribed velocity and resisting force boundary conditions and typical geometry discretisation
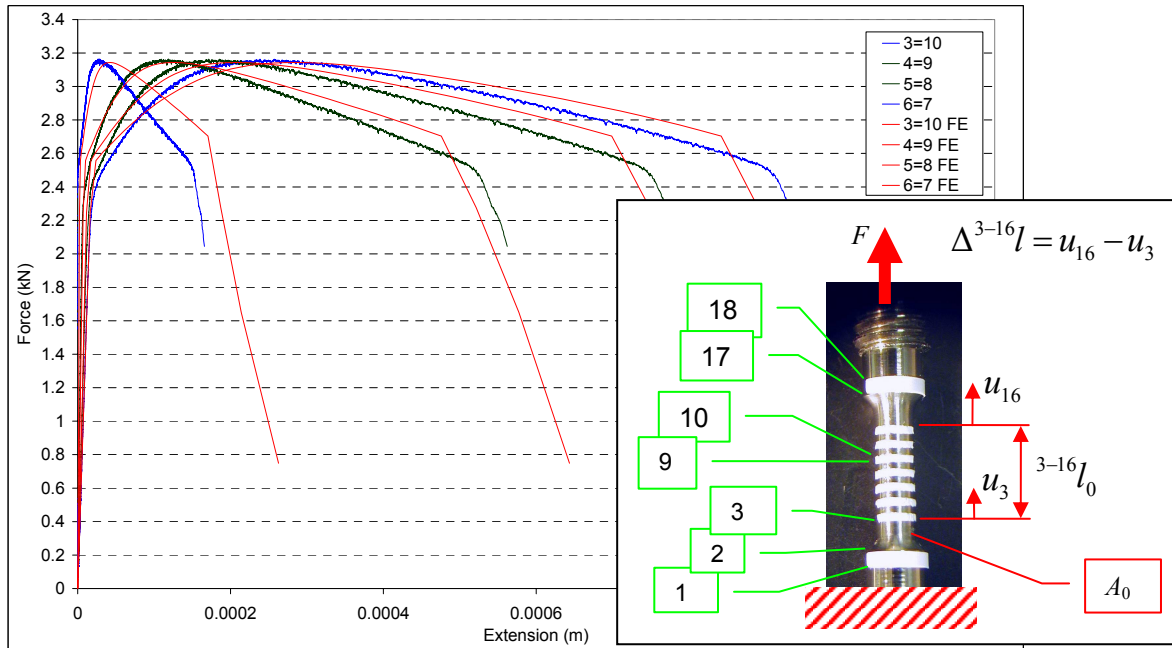
Figure 26: Typical set of results of simulations of quasi-static uniaxial tension tests
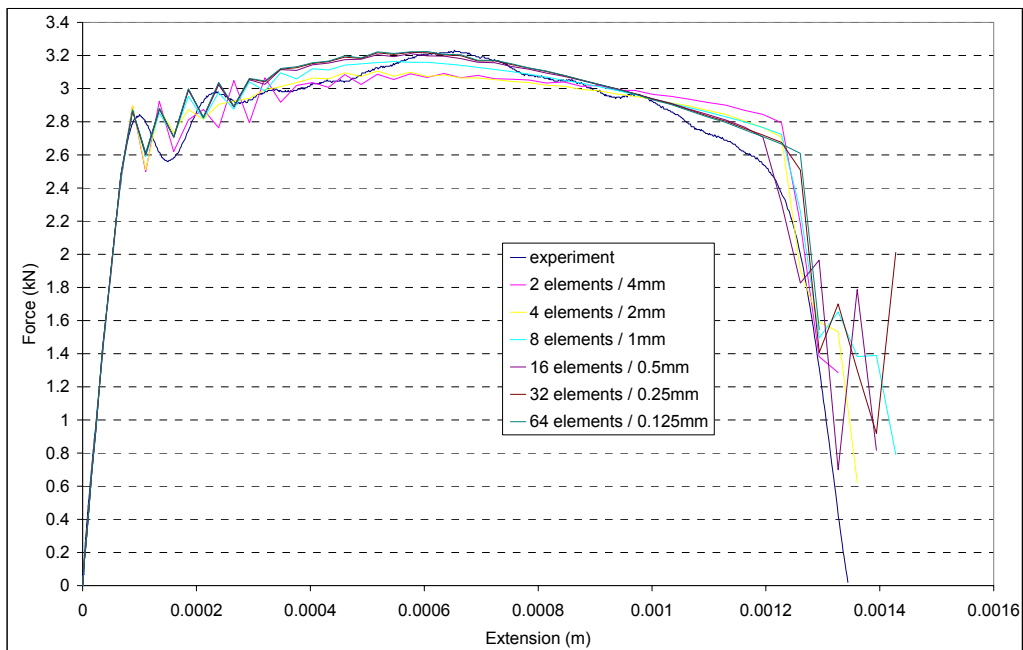

Figure 27: Typical set of results of simulations of high rate uniaxial tension tests

The comparison of results of numerical analyses of fast crack growth phenomena with experimental results is presented in *Figure 28*. The analyses showed that the crack tip velocity rapidly increased over the first 6 mm after which the crack continued to propagate at a constant velocity for another 50 mm. Both 2D and 3D numerical simulations performed were successful at accurately simulating this behaviour. However, the loss of load carrying capability is accompanied by a rapid increase in crack propagation velocity in the last 40 mm which the numerical models were not able to follow with the same level of accuracy [12].
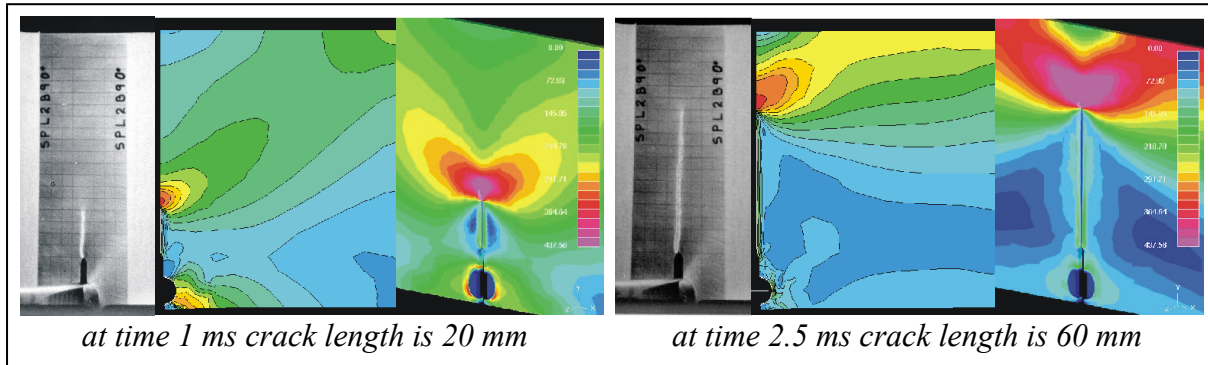
| at time 1 ms crack length is 20 mm | at time 2.5 ms crack length is 60 mm |

Figure 28: Comparison between experimental and results of 2D and 3D numerical simulations

The results of simulation of low velocity plat impact bending experiments enabled comparisons of total forces (applied and transmitted by the specimen) against laboratory experiments (*Figure 29*, *Figure 30*). Further studies involving detailed measurements of the deflected shape are planed.
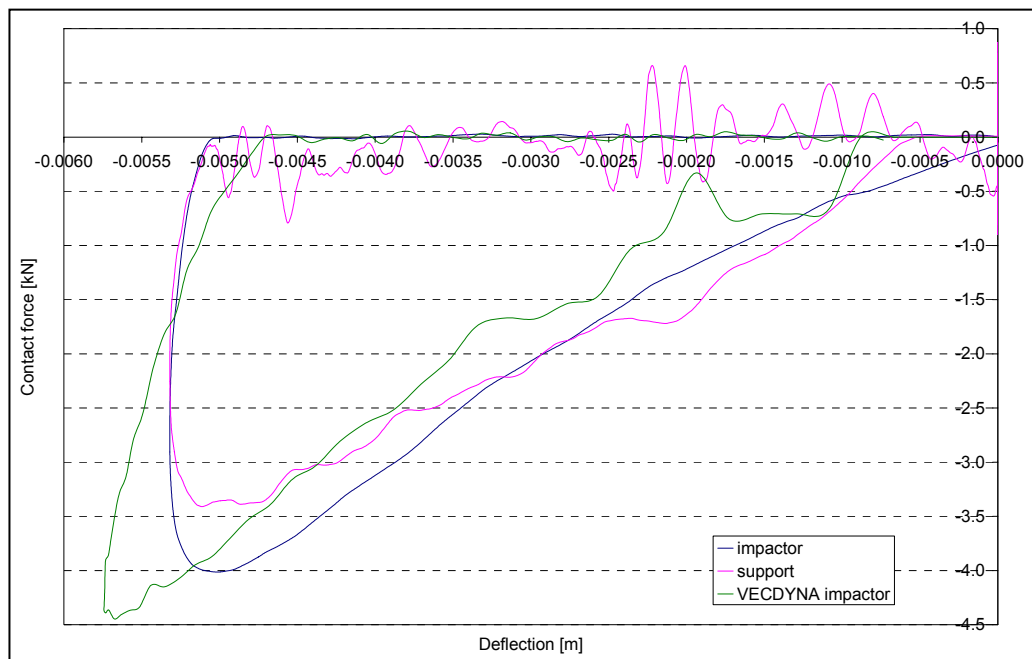

Figure 29: Typical set of results of simulations of low velocity plate impact bending tests
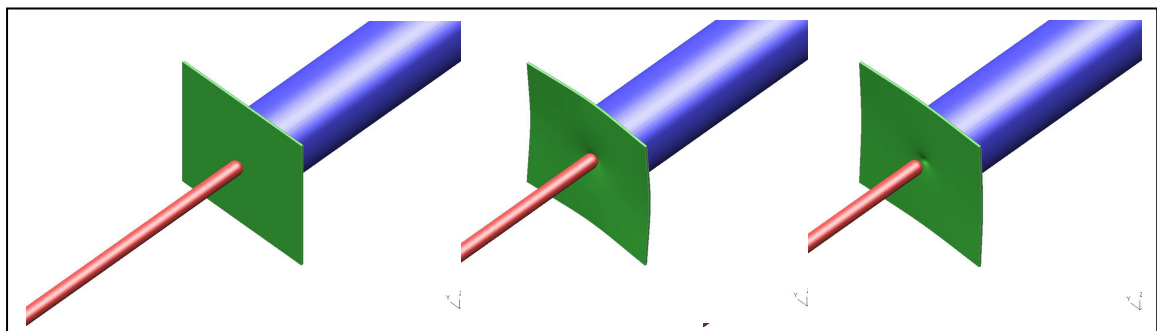

Figure 30: Typical set of results of simulations of low velocity plate impact bending tests

The results of medium velocity impact penetration experiments are illustrated in terms of simulated projectile slow-down and the corresponding impact force as functions of time (*Figure 31*). Fracture patterns obtained numerically (*Figure 32*) show good correlation with experimental results (*Figure 20*).
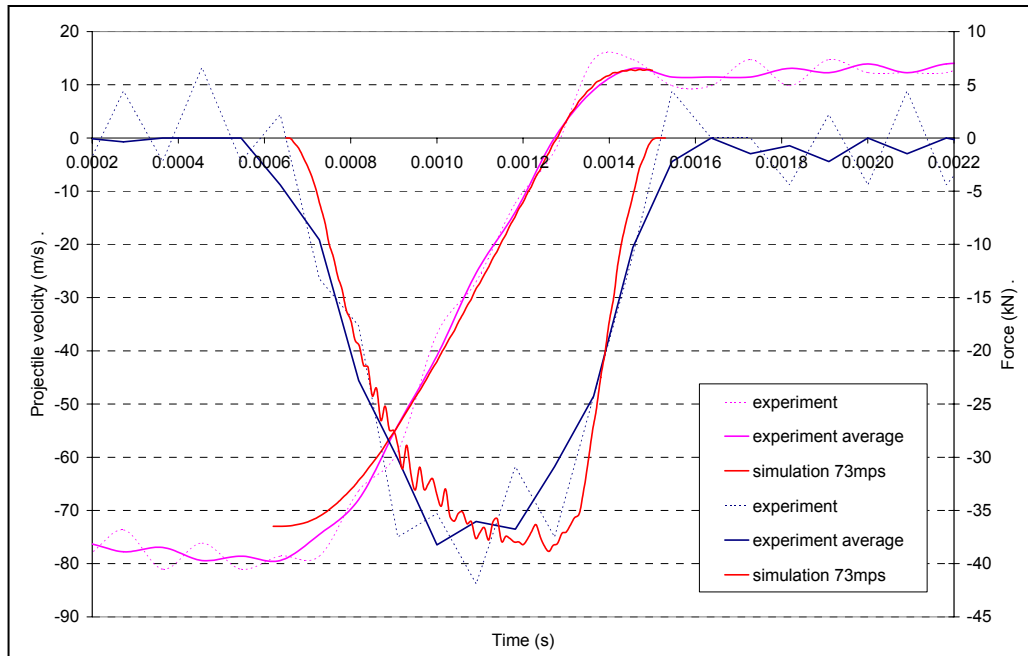

Figure 31: Typical set of results of simulations of medium velocity plate impact tests (conical projectile)
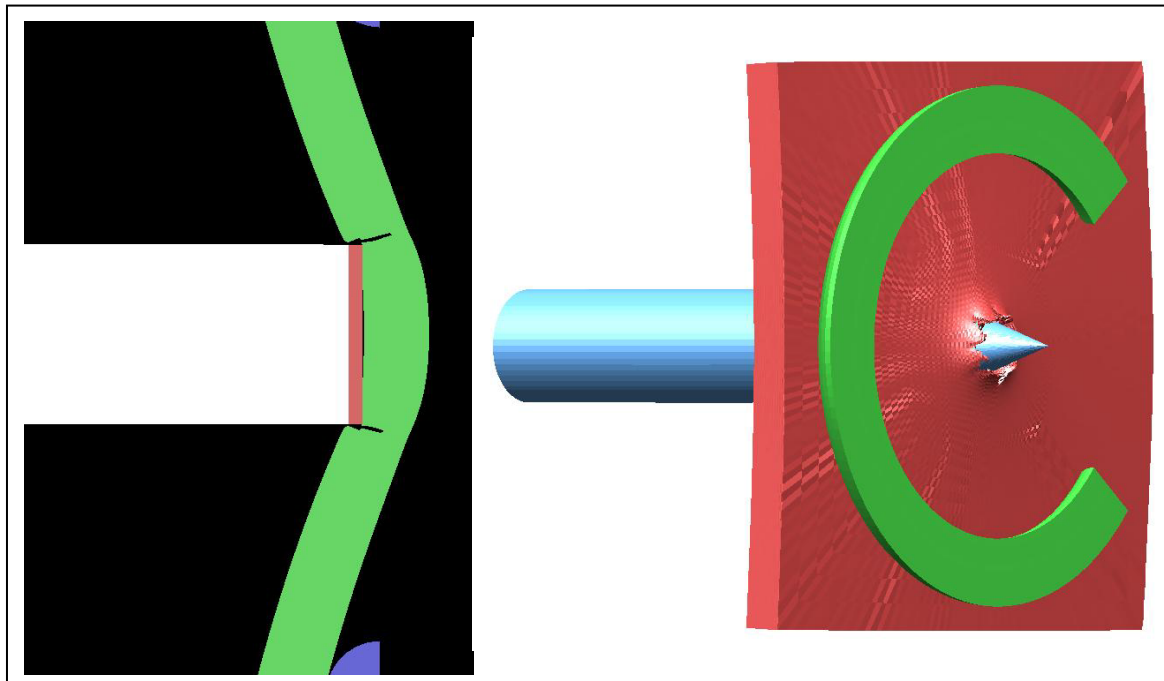

Figure 32: Numerically simulated fracture patterns

ELEMENT SPLITTING METHOD FOR SIMULATION OF FRACTURE

The most commonly used algorithms for simulation of material fracture by means of the finite element method are based on the element removal technique illustrated in *Figure 33*. The main shortcomings of such approach lie in crack blunting and highly mesh dependent predictions of crack propagation both in terms of crack orientation and velocity of crack propagation (even though the sketch in *Figure 33* suggests the opposite). In addition, removing elements strongly influences the results in case of crack opening modes II & III where an accurate modelling of crack closure or energy dissipation due to sliding along the created contact surfaces is particularly important.
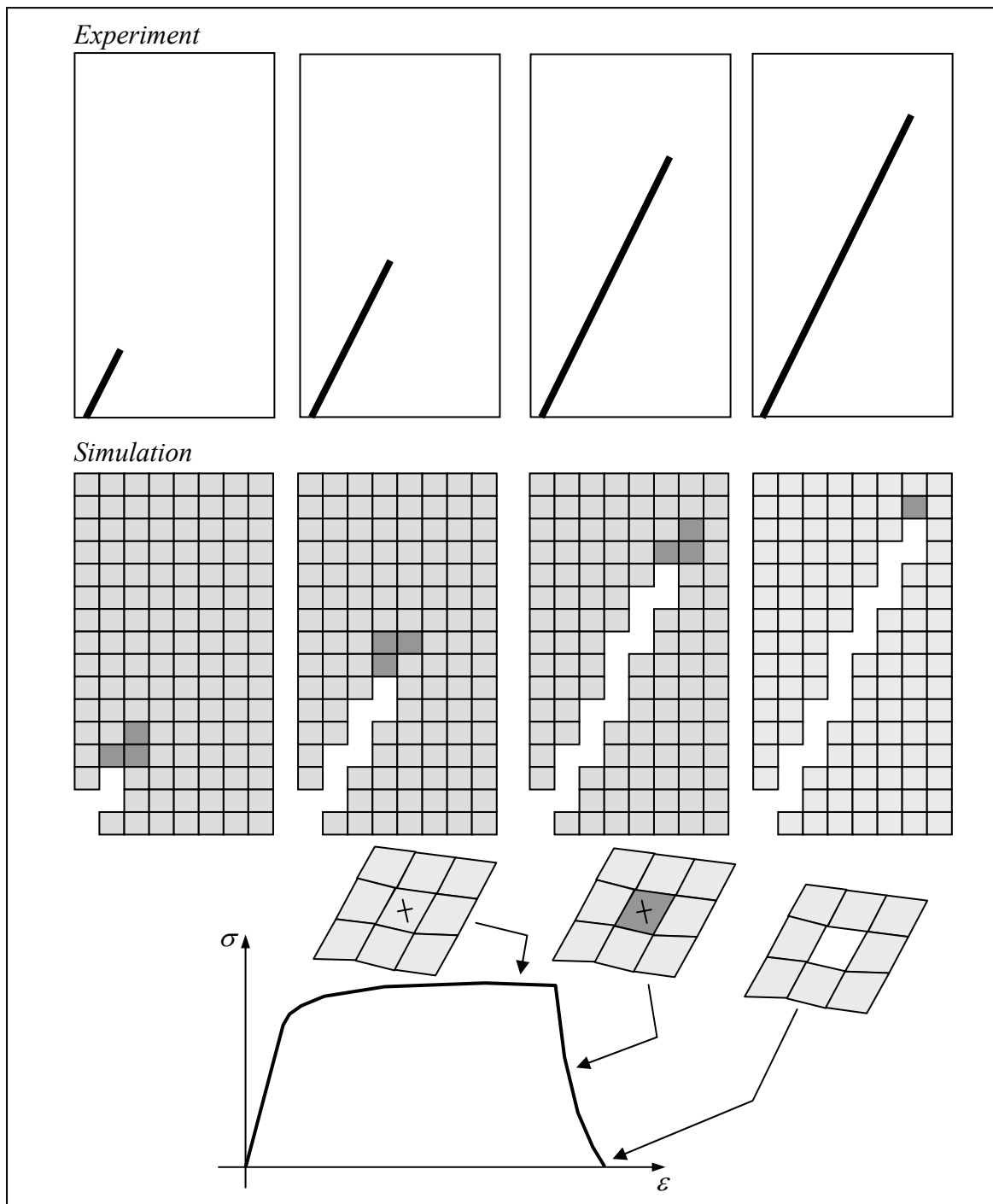

Figure 33: Element removal technique

An improved predictive modelling of crack initiation and propagation in shells and solid continua should therefore be based on an element splitting method. In this paper the focus has been placed on explicit solutions of partial differential equations describing the dynamic equilibrium of solid bodies subjected to impact loading. Such simulations are mostly performed by employing constant strain or underintegrated finite elements. As a result, extreme values of all fields (e.g. displacement, velocity, strain, stress, etc.) evaluated during the course of simulation are found at nodal positions. Consequently, it is correct to expect that the cracks should initiate at nodes. Once a crack appears the affected elements are split or adapted by inserting new nodes at the crack tip and rearranging element topologies. In 3D solid continua the crack front appears after initiation as a polygon connecting a number of nodes at the tip (*Figure 40*).

In this approach to simulation of cracking in solid domains discretised by finite elements a quasi non-local technique is used for determination of crack orientation at nodal points by averaging the material states from surrounding elements. In case of thin sheet geometries discretised by shell elements both elements along the potential path of the crack have to cease to resist further to continuing deformation before the crack can be initiated using the averaged information on the crack orientation from all elements sharing the node under consideration (*Figure 34*).
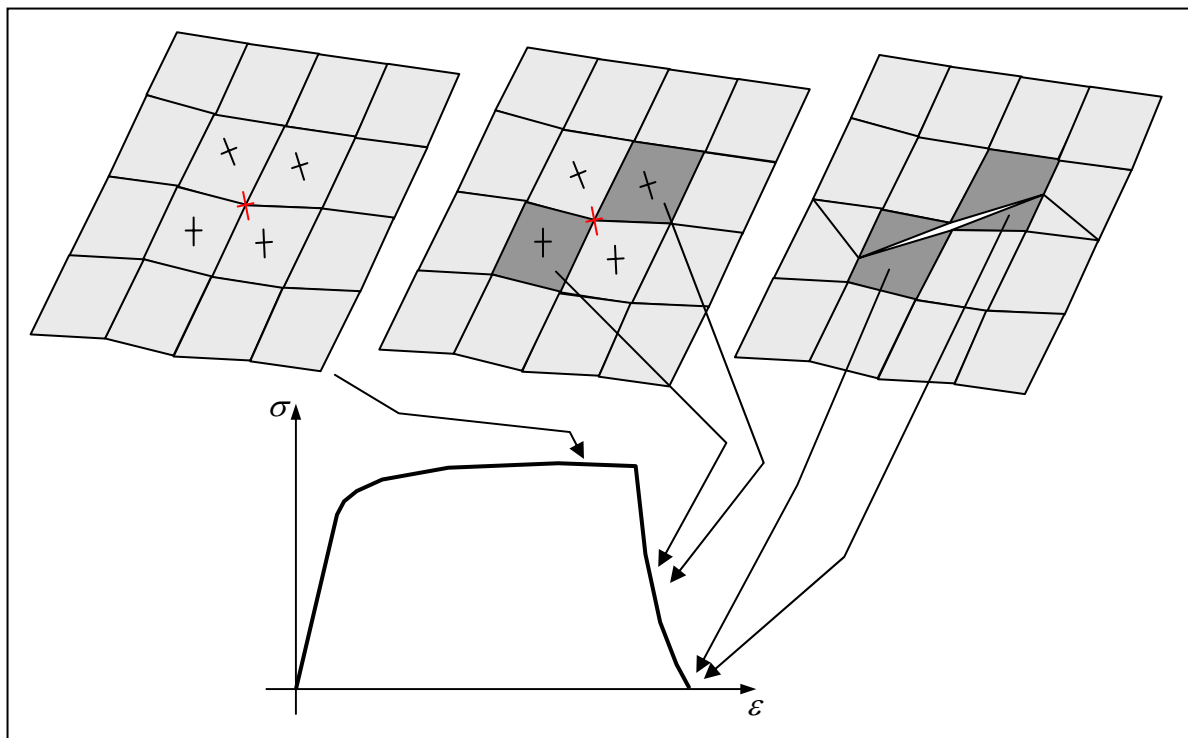

Figure 34: Node based splitting technique

The crack propagation is simulated by repeating the same procedure at subsequent time steps of the solution process at nodal points shared by elements in which the onset of softening is detected (*Figure 35*). It is clear that this approach ensures that the crack orientation and velocity of crack propagation are virtually unaffected by element size or orientation. The only restriction upon the crack orientation is imposed by the size of elements generated following crack initiation whereby very small newly generated elements can cause an unacceptable reduction in size of the time increment used in the time stepping scheme for solving the underlying equilibrium differential equations. The size of the time increment can be kept at the same size by either scaling the element properties or by

modifying the direction of the crack in such way that it connects to the nearest node at the opposite side of the element being split (*Figure 36*).
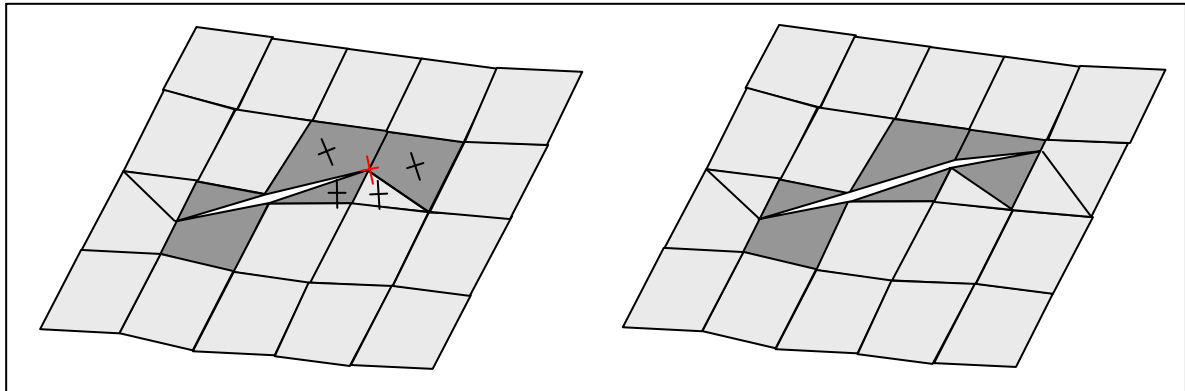

Figure 35: Node based splitting technique and mesh independent continuous crack path
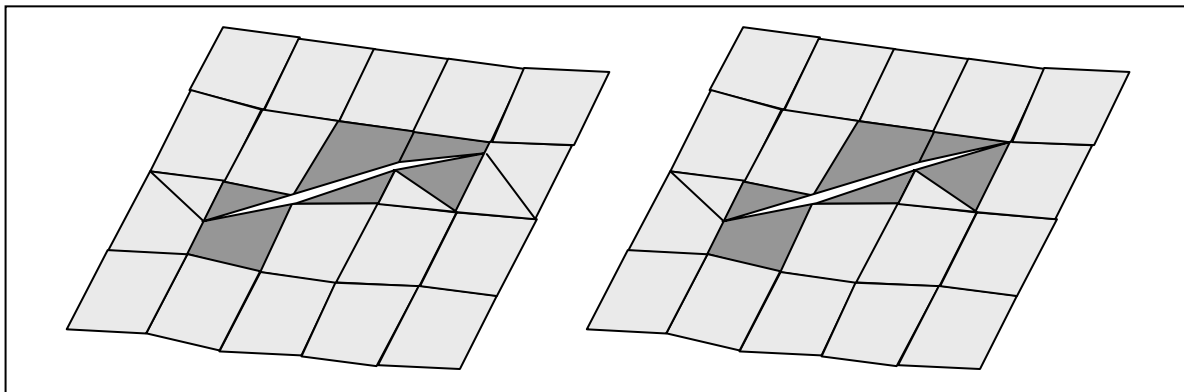

Figure 36: Modification of crack orientation to avoid generation of small elements and thus caused reduction of time increment

The node based element splitting provides unique ability to simulate the crack propagation independently of the mesh size and alignment thus enabling accurate prediction of mixed mode crack bifurcation as illustrated in *Figure 37*.
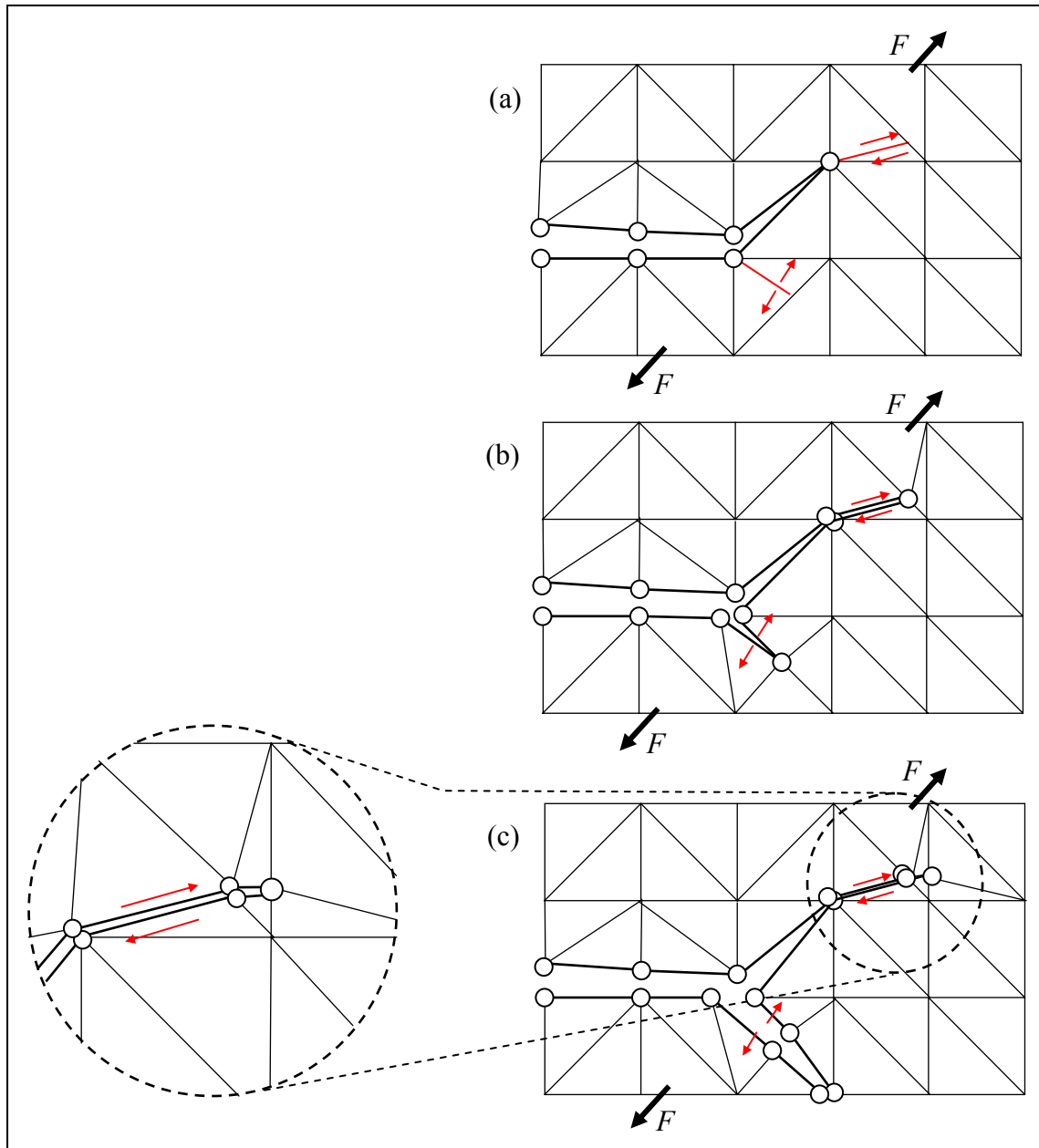
Figure 37: Element splitting simulation of simultaneous mode I and mode II crack propagation

Element splitting of 3D solid continuum elements is generic but the complexity of its implementation is dramatically higher because there can be more than just two neighbours sharing an element edge. The procedure is illustrated as per the implementation in the Oxford Solid Mechanics Group DEST (Discrete Element Simulation Tools) software.
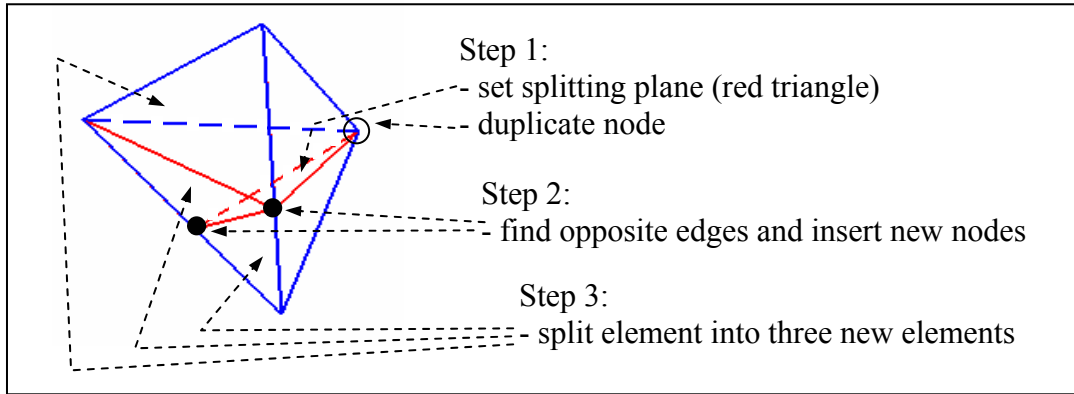
Step 1:
- set splitting plane (red triangle)
- duplicate node

Step 2:
- find opposite edges and insert new nodes

Step 3:
- split element into three new elements

Figure 38: Splitting a single tetrahedron at a given node (denoted by open circle)

Step 1:
- set splitting plane (red triangle)
- duplicate node

Step 2:
- find opposite edges and insert new nodes

Step 3:
- split element into three new elements

Step 4:
- adapt neighbouring element to utilise the new
  nodes inserted along common element edges
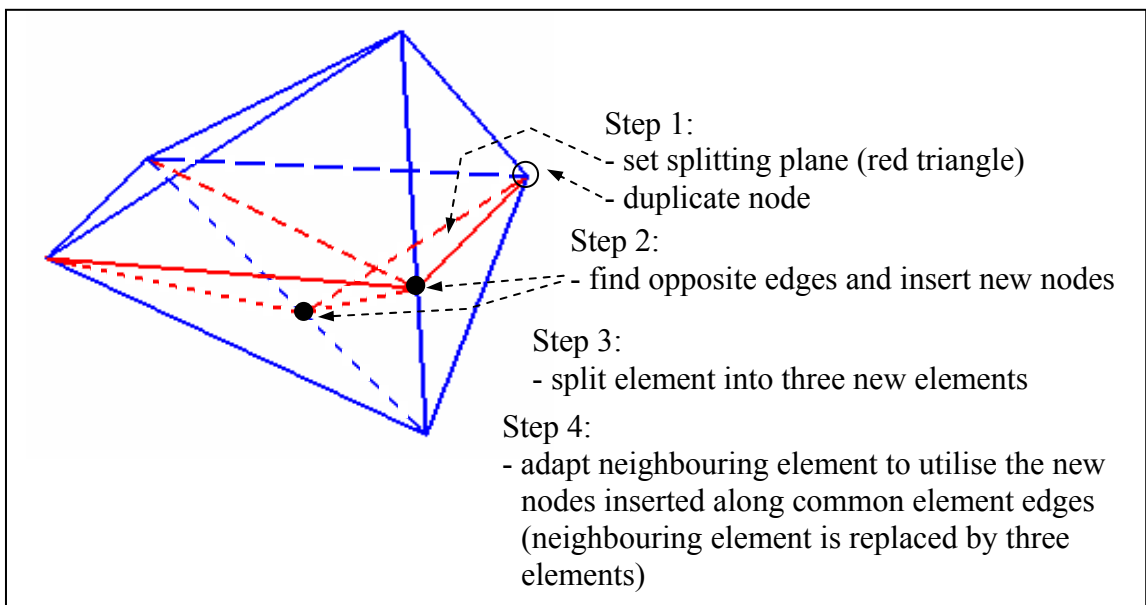 (neighbouring element is replaced by three
  elements)

*Figure 39: Splitting a tetrahedron at a given node (denoted by circle) adjacent to another
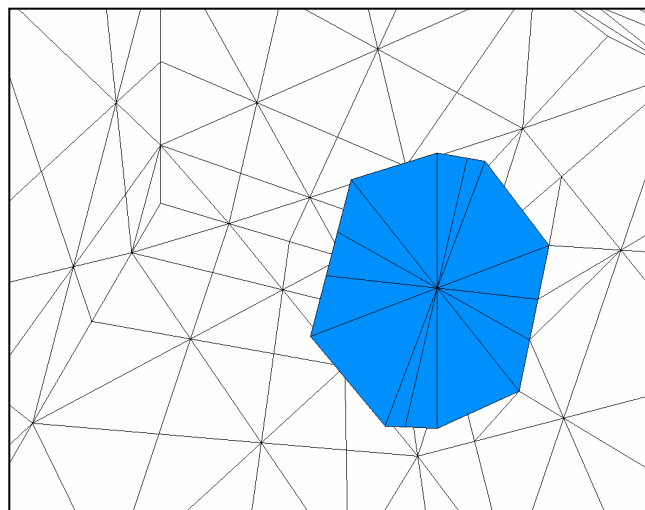tetrahedral element*

*Figure 40: View of inside of cube after initiation of the crack, only plotting faces which are
not connected to any other face, removing most edges and faces inside the cube from the
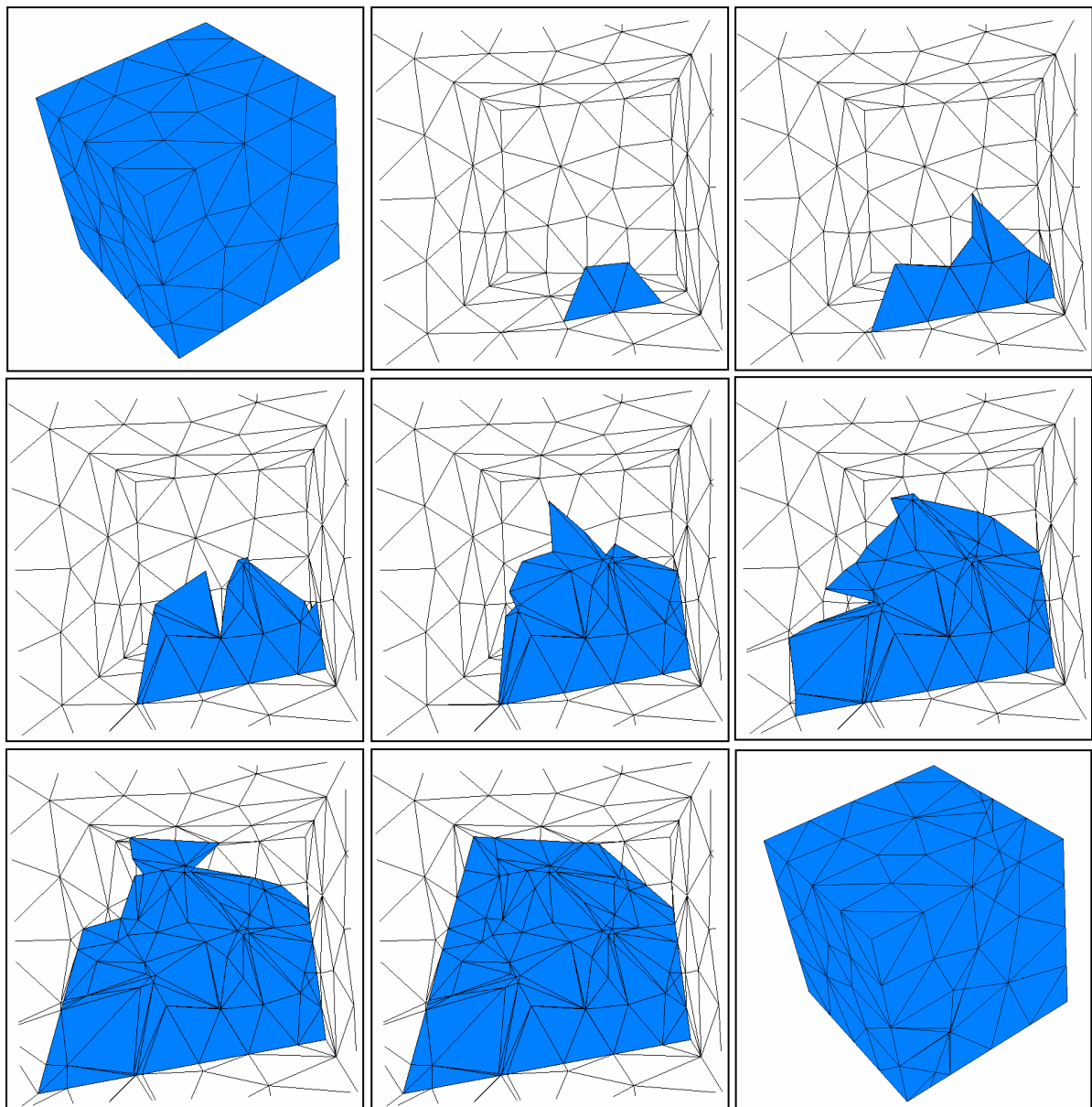view, except for the crack surfaces.*

Figure 41: Crack propagation from boundary by splitting unstructured tetrahedral mesh (view from inside of cube after initiation of the crack shows culled back-face wireframe and outer element faces along the crack plane)

CONCLUSIONS

The increased complexity of numerical modelling algorithms results in classifying all experiments as "validation tests" as it is impossible to separate concurrent mechanisms of material deformation and fracture. An integrated experimental-numerical approach to predictive modelling of material response to impact loading has been presented in which the following main aspects have been addressed

- the need to perform a multitude of experiments each of which amplifies certain aspects of material response;
- the need to simulate all classes of conducted laboratory experiments by applying measured geometry and boundary conditions;

- the need to undertake inverse modelling to identify the model parameters and validate chosen models;
- the need to employ element splitting technique for accurate simulation of material fracture illustrated by showing remeshing operations around an inserted crack plane in 3D.

Aspects of this constantly evolving methodology have been illustrated using the early results of the characterisation of an aluminium alloy for aerospace applications.

REFERENCES

1   Bammann,D.J., Chiesa,M.L., Horstemeyer,M.F., Weingarten L.I.: *Failure in ductile materials using finite element methods*; Structural Crashworthiness and Failure, (N. Jones and T. Wierzbicki, eds.); Elsevier Applied Science, London; pp.1-54; 1993

2   Belytschko,T., Liu,K.W., Moran,B.: *Nonlinear Finite Element Analysis for Continua and Structures*; John Wiley and Sons; 2000

3   Bonet,J., Wood,R.D.: *Nonlinear Continuum Mechanics for Finite Element Analysis*; Cambridge University Press; 1997

4   Dowling.N.E.: *Mechanical behaviour of materials: engineering methods for deformation, fracture and fatigue*; Prentice Hall; New Jersey; 1999

5   D. Bonnenfant, F. Mazerolle and P. Suquet: *Compaction of powders containing hard inclusions: experiments and micromechanical modelling*; Mechanics of Materials, Volume 29, Issue 2, July 1998, Pages 93-109

6   Harding,J., Noble,J.P.: *An Extended Hopkinson-bar Analysis*; UTC report 124; 1998

7   Khan,A.S., Huang,S.: *Continuum Theory of Plasticity*; John Wiley and Sons; 1995

8   Koh,C.G., Owen,E.R.J., Peric,D.: *Explicit dynamic analysis of elasto-plastic laminated composite shells: implementation of non-iterative stress update schemes for the Hoffman yield criterion*; Computational mechanics, 16, p.307-314; 1995

9   Lemaitre,J.(Editor): *Handbook of Materials Behavior Models: Volume Set*, Academic Press; 2001

10 Lemaitre,J., Chaboche,J.L.: *Mechanics of Solid Materials*; Cambridge University Press; 1994

11 Macdougall,D., Petrinic,N.: *A local optimisation method for obtaining material model parameters*; Engineering Computations; Vol.17; No.2&3; p.175-189; 2000

12 Medina-Velarde,J.L., Petrinic,N., Ruiz,C.: *Parametric Study of Ductile Crack Propagation in Aluminium Panels*; Journal de Physique IV; EURODYMAT 2000; Vol.10; p.409-414; 2000

13 N. Petrinic, L. Wang, and B.C.F. Elliott; *An Approach to Predictive Modelling of Failure in Metals Subjected to Impact Loading*, Proceedings of the 7th International Conference on Computational Plasticity COMPLAS2003, Barcelona, 7-10 Apr 2003

14 R.V. Preston, H.R. Shercliff, P.J. Withers, S. Smith; *Physically-based constitutive modelling of residual stress development in welding of aluminium alloy 2024*, Acta Materialia 52 (2004) 4973–4983